Muon Endcap Alignment for the CMS Experiment and Its Effect on the Search for Z' Bosons in the Dimuon Channel at LHC

by
Samir Guragain

Master's Degree in Physics
Central Department of Physics, Tribhuvan University
Kathmandu, Nepal
2002

A dissertation
submitted to
Florida Institute of Technology
in partial fulfillment of the requirements
for the degree of

Doctor of Philosophy
in
Physics

Melbourne, Florida
December 2010

© Copyright 2010 Samir Guragain
All Rights Reserved

The author grants permission to make single copies

We, the undersigned committee, hereby recommend that the attached document be accepted as fulfilling in part the requirements for the degree of Doctor of Philosophy in Physics.

"Muon endcap alignment for the CMS experiment and its effect on the search for Z' bosons in the dimuon channel at LHC" -
a dissertation by Samir Guragain

Marcus Hohlmann, Ph.D.
Associate Professor, Department of Physics and Space Sciences
Major Advisor

Debasis Mitra, Ph.D.
Professor, Department of Computer Sciences
External Committee Member

Laszlo A. Baksay, Ph.D.
Professor, Department of Physics and Space Sciences
Committee Member

Terry D. Oswalt, Ph.D.
Professor and Head, Department of Physics and Space Sciences
Committee Member

Ming Zhang, Ph.D.
Professor, Department of Physics and Space Sciences
Committee Member

ABSTRACT

Muon endcap alignment for the CMS experiment and its effect on the search for Z' bosons in the dimuon channel at LHC

by

Samir Guragain

Dissertation Advisor: Marcus Hohlmann, Ph.D.

The first 7 TeV proton-proton collisions produced by the LHC have been recorded by the CMS experiment in 2010. The CMS muon endcap alignment system succeeded in tracking muon detector movements of up to 18 mm and rotations of a few milliradians under magnetic forces during the system commissioning at full magnetic field in 2008. This dissertation describes in detail the reconstruction of chamber positions from alignment data. The system achieved chamber alignment precisions of 220 - 340 μm and 200 μrad. Systematic errors on displacements are estimated to be less than 500 μm.

This dissertation describes the expected effect of muon misalignments on the search for $Z' \rightarrow \mu^+\mu^-$ using fully reconstructed sets of simulated events of proton-proton collisions at $\sqrt{s} = 7$ TeV with the CMS experiment. The simulation results show that the expected p_T resolution for muons in the end-

cap is about 14.4% (4.8%) with the startup (ideal) alignment scenario using a 1.2 TeV/c^2 Z' sample. The impact of systematic biases in the muon endcap positions and rotations on the p_T resolution is also studied and quantified. Using the Monte Carlo samples, the discovery potential for Sequential Standard Model Z'_{SSM} with different muon misalignments and integrated luminosities is evaluated. A CMS detector better aligned than with the current startup alignment requires significantly less data.

Preliminary results for dimuon events using ~ 300 nb^{-1} of first collision data at $\sqrt{s} = 7$ TeV with the CMS experiment are presented.

Acknowledgments

Firstly, I express my sincere thanks to my mentor and dissertation supervisor, Professor Marcus Hohlmann for his continuous guidance, training, and all possible support throughout my graduate study and research work. I would like to mention my dissertation committee members Professors Laszlo A. Baksay, Debasis Mitra, Terry D. Oswalt, and Ming Zhang for their support and time amidst their busy schedules. Professor Hamid Rassoul's encourgement throughout the period is worth mentioning here. I would also like to thank my ex-committee members: Professors Stephane Vennes and James Mantovani, who gave me the comprehensive exams and also taught courses here.

I am thankful to my friends Patrick Ford, Himali Kalakhety, Hamit Mermerkaya, Robert Michael Ralich, Lucille Serody, Robert Serody, and office mate Dr. Kondo Gnanvo for their friendship, encouragement, and help. Also, I would like to thank staffs, especially the late Irene Nash and Elaine Carlyle from the department of physics and space sciences in Florida Instiute of Technology for providing me numerous administrative helps.

I would like to extend my gratitude to Drs. David Eartly, Oleg Prokofiev, James Bellinger, Jim Pivarski, Jordan Tucker, Xiaofeng Yang, Teresa Rodrigo,

Piotr Traczyk, Martijn Mulders, Meenakshi Narain, and Gervasio Gomez for their technical assistance, scientific consultation, and advice during various stages of this work.

I am also indebted to the CMS collaborators, authors, laboratories mainly CERN and Fermi National Lab., and publishers cited in this dissertation. The continuous financial support from the department of physics and space sciences in Florida Institute of Technology and the US Department of Energy gave me the peace of mind to study and complete this dissertation work.

I would like to remember professors Mukunda Mani Aryal, Shekhar Gurung and Pradeep Raj Pradhan from Tribhuvan University, Nepal along with other teachers who taught me during the last 24 academic years. Without their efforts, I would not be at this position.

Lastly, I must express deep gratitude to my family especially my lovely wife, Anisha and, my cute and innocent daughter, Safiya, for their patience, forbearance, encouragement, and smiles.

Dedication

To my parents, the late Shanti Ram Guragain and Laxmi Devi Guragain, who always wanted their children to be better educated than themselves.

Contents

List of Figures

List of Tables

Chapter 1

Introduction

The elementary constituents of matter and their fundamental interactions are described by the Standard Model (SM) [1, 2] and it has been tested by several experiments with a high precision. The experiments at the Large Electron-Positron (LEP) [3] and the Fermilab Tevatron [4] colliders are the most relevant to this dissertation. In particular, the yield of lepton pairs produced mainly via Drell-Yan (DY) processes, i.e. quark (q) - antiquark ($\overline{q}$) annihilation by exchange of photons or Z^0 bosons, is predicted by the SM with high confidence. So far, the experimental data have shown no significant deviation from the SM predictions for the Drell-Yan continuum up to energy scales of several hundred GeV/c^2. However, many models for new physics predict various violations of the standard behaviour of SM spectra and, therefore, their testing at a new energy scale is one of the priority tasks of particle physics. The most direct way

is to look for effects of new physics in the form of individual resonances above the Drell-Yan continuum. This strategy is motivated by predictions coming from various left-right symmetric models, extended gauge theories including grand unification theories, models of composite gauge bosons [5, 6], or extra dimension scenarios. In all these cases, neutral gauge vector (Z') bosons are expected to appear at a mass scale of the order of one to several TeV/c^2. Such Z' bosons typically couple with electroweak strength to SM fermions, and can be observed at the Large Hadron Collider (LHC) as narrow, spin-1, dimuon resonances from $q\overline{q} \rightarrow Z' \rightarrow \mu^+\mu^-$.

These studies can be performed with the Compact Muon Solenoid (CMS) experiment at LHC. The primary goal of the Compact Muon Solenoid (CMS) experiment [7] is to explore particle physics at the TeV energy scale exploiting the proton-proton collisions delivered by the Large Hadron Collider [8]. Precise measurement of muons up to the TeV/c momentum range requires the muon chambers to be aligned with respect to each other, and to the central tracking system, with precision of a few hundred microns in position and about 40 microradians in orientation [9]. In addition, the effect of muon alignment has a stronger dependence on momentum at these scales because long lever arms are needed to resolve small track curvatures. While the expected misalignment does not generally affect the distribution of Drell-Yan backgrounds up to higher masses, there is a small broadening of the resonance peak that could reduce the

statistical significance of a potential discovery. In this dissertation, mainly the effect of muon alignment on the search for Z' gauge bosons in the $Z' \to \mu^+\mu^-$ decay channel with pp simulated collision events at 7 TeV with CMS is presented.

This dissertation is organized as follows: the first chapter briefly reviews the theoretical framework and introduces the model with heavy resonances decaying to dimuons in the CMS experiment at the LHC. The second chapter is devoted to a brief overview of the LHC and the CMS detector with emphasis on muon alignment. In the third chapter, the muon endcap system and its alignment are described. In the same chapter, the alignment procedure to produce the alignment constants, which are used to define the muon geometry for the track reconstruction, is presented. The fourth chapter describes a Z' analysis with simulated data and the effect of misalignment on the p_T resolution and hence the mass resolution for high-mass resonances. It is shown how muon alignment affects the resolutions in the search for a narrow resonance and the calculation of Z' signal significance. The fifth chapter contains data analysis from the recent proton-proton (pp) collisions at $\sqrt{s} = 7$ TeV with the CMS experiment and summarizes the preliminary results in the dimuon channel. In the last chapter, the main results of the present work are summarized and the future direction of this work is outlined.

1.1 The Standard Model and Elementary Particles

There are four known fundamental interactions between particles. These interactions are gravitational, weak, electromagnetic, and strong. While the unification of these four interactions into one model, theory, or a set of equations has long been the aim of physicists, this has not yet been achieved, although progress has been made in the unification of the electromagnetic and the weak interactions. The Standard Model (SM) [1, 2] of particle physics best decribes the three fundamental interactions between the elementary particles that make up all matter, but does not explain gravitational interaction.

Gauge theories explain fundamental interactions. A gauge theory involves a symmetry group for the fields and potentials known as the gauge group. The gauge group of strong interaction is SU(3) and the gauge group of electroweak interaction is $\mathrm{SU}(2) \times \mathrm{U}(1)$. In other words, SU(3) represents quantum chromodynamics (QCD), the theory of strong nuclear interactions, and $\mathrm{SU}(2) \times \mathrm{U}(1)$ is the unified electroweak (sometimes called quantum flavordynamics, QFD) theory which describes electromagnetic (EM) and weak nuclear interactions as different manifestations of a single system. The gauge groups $\mathrm{SU}(3) \times \mathrm{SU}(2) \times \mathrm{U}(1)$ represent the electroweak theory and quantum chromodynamics. All of these theories are gauge theories, meaning that they model

the forces between fermions by coupling them to bosons called gauge bosons, which mediate the forces.

In the Standard Model, elementary particles are leptons, quarks, and force carriers (mediators). The leptons and quarks are fermions with spin 1/2. They are summarized in Table 1.1. They are divided into three distinct generations. The generations are organized by increasing mass. Quarks are distinguishable from leptons in that they interact via the strong force.

Table 1.1: Properties of the Standard Model fermions with spin 1/2. The index, i, on each quark runs from 1 to 3 and represents its color.

Fermions	Generation I II III	Charge (e)	Interaction
leptons	$e \quad \mu \quad \tau$	-1	EM, Weak
	$\nu_e \quad \nu_\mu \quad \nu_\tau$	0	Weak
quarks	$u_i \quad c_i \quad t_i$	$+\frac{2}{3}$	Strong, EM, Weak
	$d_i \quad s_i \quad b_i$	$+\frac{1}{3}$	Strong, EM, Weak

All force mediators are bosons. Bosons, summarized in Table 1.2, mediate three of the four known forces. The interaction of the particles is mediated via the exchange of bosons: the photon (γ), the W, Z, and the gluons (g), which are the mediators of the electromagnetic, weak, and strong forces, respectively.

These bosons have spin 1.

Table 1.2: Properties of the Standard Model interaction mediators, the gauge bosons with spin 1.

Interaction	Range	Mediator	Charge (e)	Mass (GeV)
Weak	∞	Z^0	0	91.2
		W^-	-1	80.4
		W^+	$+1$	80.4
EM	10^{-18} m	γ	0	0
Strong	10^{-15} m	gluon, g (8)	0	0

The coupling strength of the EM interaction is $\alpha \approx 1/137$ at low energies, but increases as the energy increases. The theory of the EM interaction was independently formulated first as quantum electrodynamics which showed a remarkable agreement with the experimental observations. Since QED itself is a unified theory of electricity and magnetism, the next step was to include another type of force.

The mediators of the weak forces are required to be massive, otherwise the cross section of the weak interaction diverges to infinity. The weak interaction is unique in that it violates parity which is conserved in the EM and strong interactions. The different EM and weak interactions are successfully incorporated

in the unified EW theory where the photon and the weak bosons are represented as combinations of four gauge fields required by the SU(2) $\times$ U(1) local gauge theory.

A characteristic of the strong interaction is that the coupling constant decreases with energy and increases with distance asymptotically. Hence, the quarks are only observed as bound state hadrons. Another consequence of the quark confinement is that forcing the quarks to large separation by enough energy leads to the creation of quark-antiquark pairs. In QCD, these phenomena are explained in terms of color, where all observable stable states must be color singlets. Each quark flavour may take one of the three colors, red(r), green(g) or blue(b), and a stable hadron must be a colorless combination of these quarks. Gluons are represented as combinations of two colors such that the eight gluon states form an SU(3) octet, hence are not observable as free particles. In total, the SM describes thirty-seven elementary particles: eighteen quarks, six leptons, twelve mediators, and one Higgs boson (not discovered yet).

1.2 Physics Motivations for Z'

The Standard Model (SM) is the current theory of quarks and leptons and their electromagnetic, weak, and strong interactions. However, it is not a complete theory because it has left many important questions unanswered: Why are the

quarks arranged in generations? Why are there four different forces? How do we unify gravitation with the other forces? There are new theories that try to address these questions. As these theories attempt to answer these questions, they often predict extremely short-lived particles called "resonances". The theory of compositeness attempts to explain the reason behind quark families by proposing a composite structure for quarks and postulates the existence of excited quarks. Grand unified theories (GUT) address the question "Why are there different forces?" and in doing so, they require new heavy bosons, typically referred to as "W'" and "Z'" bosons. The unification of gravity with other fundamental forces, which is beyond the scope of this dissertation is generally dealt with by string theories.

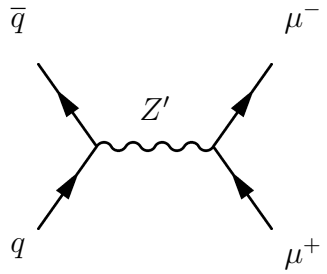

Figure 1.1: Feynman diagram for Z'

The "sequential" SM extends standard model SM in an attempt to unify the fundamental forces. It proposes new quarks, leptons, and gauge bosons that are sequential replicas of the known ones. The additional Z' and W' bosons are similar to the SM Z and W except that they are heavier. The Z' has the same

coupling for as the ordinary Z. Other Z' models are GUT, left-right, and string-motivated. In each case, the Z' couples to g'Q, with g' the U(1)$'$ gauge coupling and Q the charge. Figure 1.1 shows a typical Feynman diagram for Z'.

As the SM Z boson, the Z' is expected to be a very short-lived particle. It can only be observed through its decay products. The energy of the colliding particles must be high enough to produce a Z'. The decay products of the Z' must be then detected above the SM background. Such a background is always present because the SM Z boson and the photon are produced by the same processes which create a Z'.

The cleanest signal of Z' is the decay to opposite-signed muons [10]. The experiments at the LHC are going to be the first opportunity to search for neutral gauge bosons Z' (spin 1) in a high-mass range significantly larger than 1 TeV/c^2. The current lower mass limits for Z' is 1030 GeV/c^2 [4]. Experimentally, the $Z' \rightarrow \mu^+\mu^-$ channel is one of the most promising for Z' discovery because it has a clear signature, low background, and sizable branching ratio. It is also a good benchmark channel for the muon detector because it allows one to assess the reconstruction of very high p_T muons, detector misalignment, magnetic field uncertainties, calibration uncertainties, etc.

In this dissertation, a Monte Carlo study of a generic search for new Z' resonances which decay to dimuons with the Sequential Standard Model (SSM) in the CMS experiment is presented. It will be demonstrated that a $5\,\sigma$ dis-

covery of a multi-TeV dimuon resonance is possible at 7 TeV center-of-energy pp collision and the impact of muon alignment on the Z' signal significance is significant.

1.3 Current Limits from Previous Z' Searches

The current lower mass limits for Z'_{SSM} are 1030 GeV/c^2 and 1023 GeV/c^2 in the dimuon and dielectron channels, respectively, from the Tevatron results [4, 11]. The cross section times branching ratio in dimuons from the Tevatron for different models of Z' can be seen in Figure 1.2 (from Ref. [4]). The LHC will be the machine to explore Z' at higher mass.

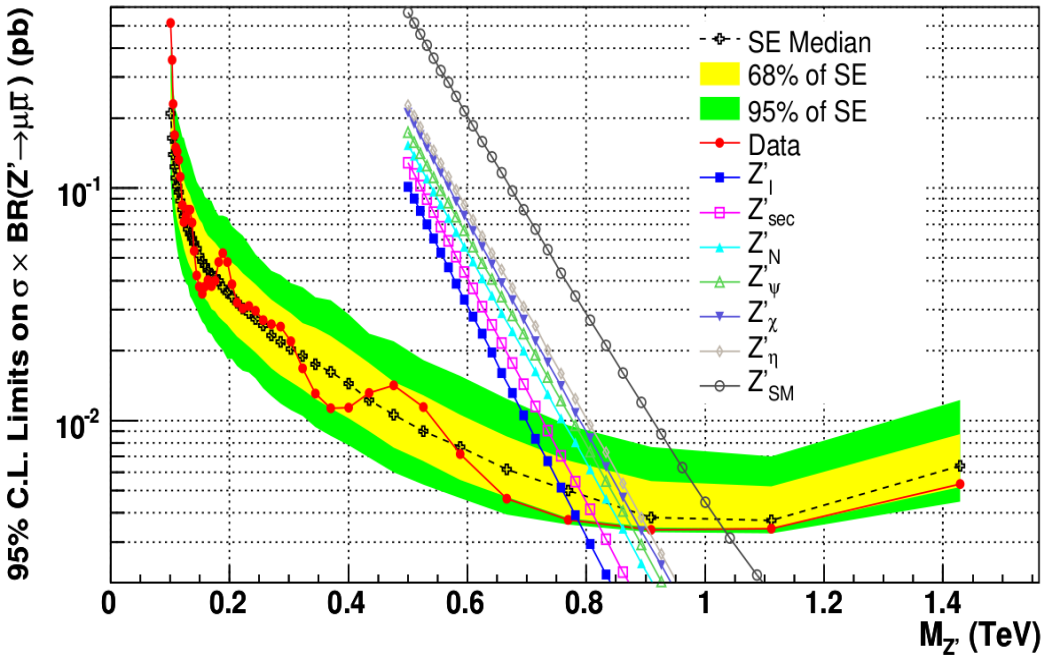

Figure 1.2: Tevatron limit for various Z' models.

Chapter 2

The CMS Experiment at the LHC

In this chapter, I summarize the main features of the Large Hadron Collider (LHC) and one of its experiments, the Compact Muon Solenoid (CMS), with an emphasis on muon system and its alignment. Details on the Large Hadron Collider (LHC) and the Compact Muon Solenoid (CMS) can be found elsewhere [8, 12] and [7, 9], respectively.

2.1 The Large Hadron Collider

The Large Hadron Collider (LHC) [8, 12] is the biggest proton-proton (p-p) collider ever built. It is located at the European Organization for Nuclear

Research (CERN) near Geneva, where it spans the border between Switzerland and France. It is a particle accelerator designed to study the smallest known particles - the fundamental building blocks of all matter.

Two beams of accelerated protons travel in opposite directions inside the circular tunnel with a circumference of 27 km and up to 175 meters below the surface. The two high energetic proton beams collide in bunches at four nominal interaction points. LHC recreates the conditions just after the Big Bang, by colliding the two beams head-on at center-of-mass energy $\sqrt{s} = 14$ TeV [13]. At present the proton beams are colliding at a reduced center-of-mass energy $\sqrt{s} = 7$ TeV and it will remain the same until 2011. By 2013 with an upgrade the collisions will be at the nominal center-of-mass energy $\sqrt{s} = 14$ TeV.

The schematic diagram of LHC with its experiments and pre-accelerators is shown in Figure 2.1 (from Ref. [14]). The six experiments at the LHC are all run by international collaborations. Each experiment is distinct and characterized by its unique particle detector [15]. The two general purpose detectors: Compact Muon Solenoid (CMS) [16] [17] and A Toroidal LHC ApparatuS (ATLAS) [18] and two other special-purpose detectors: Large Hadron Collider beauty (LHCb) [19] and A Large Ion Collider Experiment (ALICE) [20] are placed at the interaction points to collect the data on pp collisions. The detectors used by the TOTal Elastic and diffractive cross section Measurement (TOTEM) experiment are positioned near the CMS detector, whereas those

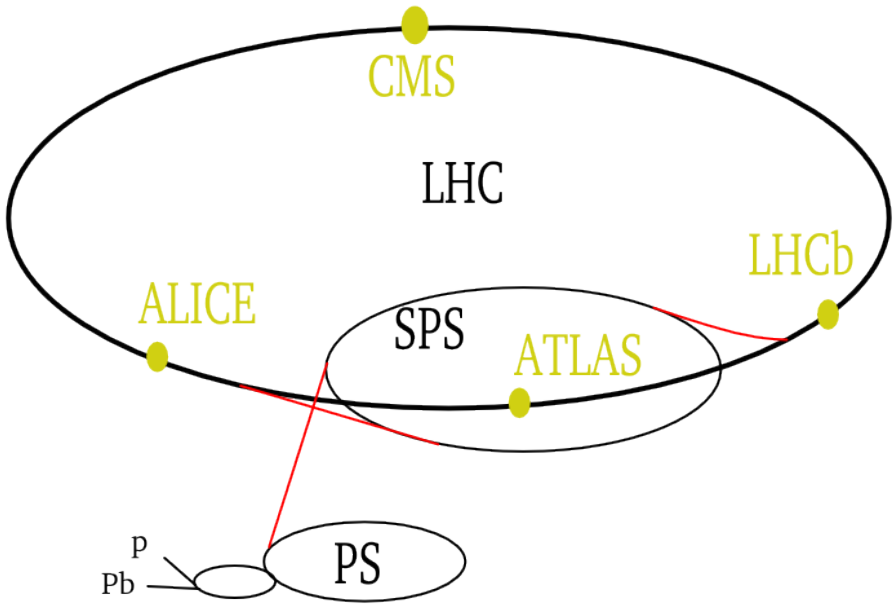

Figure 2.1: The experiments and preaccelerators at the LHC.

used by Large Hadron Collider forward (LHCf) are near the ATLAS detector.

The main objectives of CMS and ATLAS are to investigate the largest range of physics possible including the detailed measurements of Standard Model physics and beyond. Having two independently designed detectors is vital for cross confirmation of discoveries.

LHCb is specifically dedicated to the interactions of particles containing bottom quarks. The experiment is built to detect particles with a low transverse momentum (p_T) going forward close to the beam line.

The fourth detector, ALICE, is focused on studying the properties of quark-gluon plasma in heavy ion (Pb ions) collisions. This phase of matter is interest-

ing since it is believed that quarks and gluons existed as free particles during the first 20 or 30 microseconds after the Big Bang. For the heavy lead-ion (Pb-Pb) collision, the proton beams in the LHC accelerator will be replaced by lead-ion beams.

The linear accelerators (Linac2, Linac3), the booster, the low energy ion ring, the Proton Synchrotron (PS), and the Super Proton Synchrotron (SPS) are the components of the accelerator complex at LHC. First, Linac2 and Linac3 accelerate protons up to 50 MeV, then a booster provides a kick to them to 1.4 GeV. In the PS and the SPS, the protons gain energy up to 25 GeV and then up to 450 GeV, respectively. Finally the protons at 450 GeV are injected from SPS into the LHC, where two proton beams reach their nominal energy of 7 TeV each at full opeartion, resulting in collisions at a center-of-mass energy $\sqrt{s} = 14$ TeV. Each proton beam is now circulating at 3.5 TeV and hence the center-of-mass energy is $\sqrt{s} = 7$ TeV.

2.2 The CMS Detector and Its Components

The Compact Muon Solenoid (CMS) is a general purpose detector at the LHC. It is a symmetrical detector and provides nearly 4π coverage except along the beam direction. CMS is located at the interaction point 5 of LHC. The design and detector performances of CMS have been determined to meet the goals

of the LHC physics program. As its name suggests, the CMS detector has a compact design, and is specifically built to provide good muon detection and resolution. The CMS superconducting solenoid magnet generates up to 4 Tesla magnetic field (corresponding to about 2.7 GJ of stored energy) which is essential for achieving high momentum resolution and distinguishing particles in high multiplicity events. An overall picture of the CMS can be seen in Figure 2.2 (from Ref. [21]). The CMS is cylindrical in shape. The overall length and diameter of the CMS detector are ~ 22 m and ~ 15 m, respectively. It is an advanced detector made up of several sub-detectors, which are positioned in concentric layers around each other. Each is dedicated to different and complementary types of measurements.

Starting from inside to outside, the CMS detector consists of the silicon pixel and strip tracker that measures charged particle trajectories in the magnetic field and hence their momenta. Then comes the electromagnetic calorimeter (ECAL) which measures the energy of electrons and photons. Following this is the hadronic calorimeter (HCAL) which measures the energies of strongly interacting particles. Subsequently a superconducting coil deflects the charged particles so their momenta can be measured. Finally the muon detectors are used for muon identification and measurements of their momenta.

Particles enter the CMS through both ends of the beam pipe timed in such a way that both beams collide at its center. The outgoing particles from the

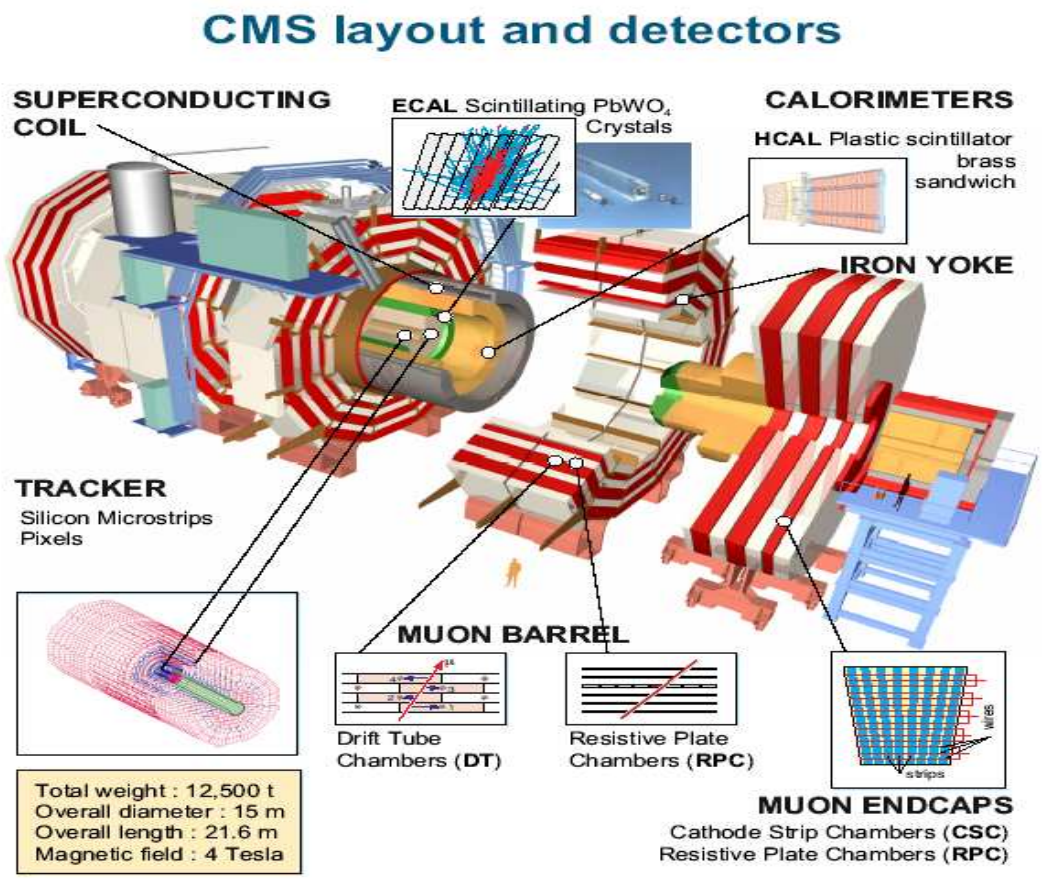

Figure 2.2: Modular design of the CMS detector showing its components: tracker, calorimeters, magnet, and muon system.

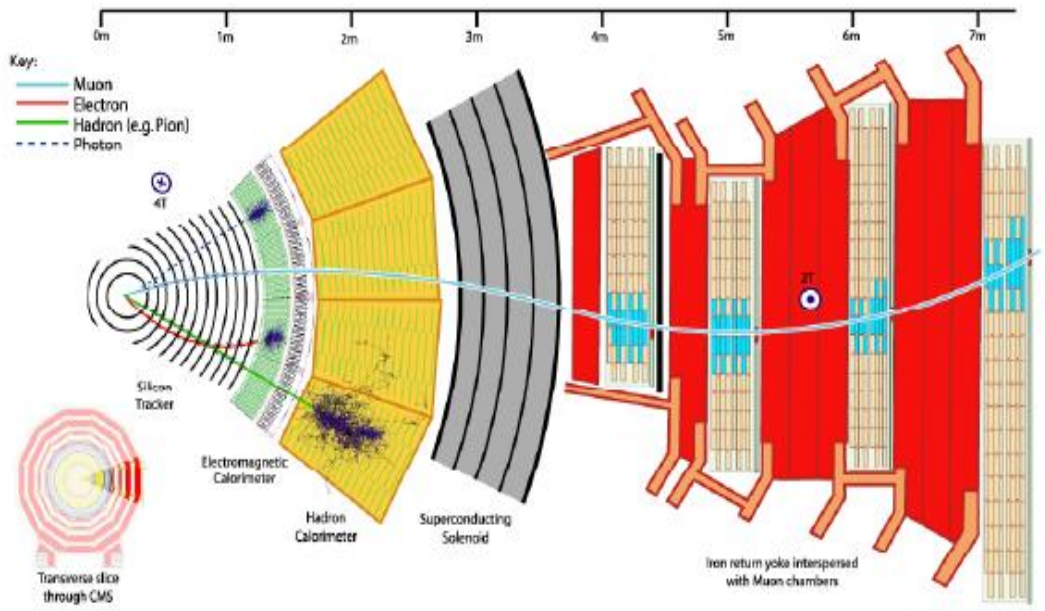

Figure 2.3: A schematic showing a transverse slice through the sub-detectors of the Compact Muon Solenoid, highlighting the paths taken by a number of particle types (muons, electrons, photons, hadrons).

interaction point then pass radially through the concentric detector layers, as shown in Figure 2.3 (from Ref. [22]).

The global coordinate system in CMS has its origin in the nominal interaction point (IP), i.e. the center of the detector. The x-axis is horizontal and points radially inward toward the center of the LHC. The z-axis is parallel to the beam axis. These two directions define the y-axis to be pointing vertically upward. The azimuthal angle ϕ is measured in the $x-y$ plane relative to the positive x-axis and the polar angle θ is defined relative to the positive z-axis. The momentum transverse to the beam direction, denoted by $p_T = p\sin\theta$ is the projection of the three-momentum on the $x-y$ plane. The pseudo-rapidity, η is defined as η = -ln(tan(θ/2)). It is a commonly used spatial coordinate describing the angle of a particle relative to the beam axis.

2.2.1 The Central Tracking System: Silicon Tracker

The innermost component of the CMS is the silicon tracker. The tracking system is designed to reconstruct high p_T muons, electrons, and hadrons with high momentum resolution and efficiency, and to measure the decay vertices of long-lived unstable particles in the CMS. The tracking system is composed of finely segmented silicon sensors (pixels and strips) which measures the momenta of charged particles and tracks them through ionization they produce along their paths. The tracker system consists of a single detector in the barrel and two

in the endcaps. In the barrel part, there are three pixel layers and ten silicon strip layers. Four of the ten silicon strip layers make the Inner Barrel (TIB) and six of them form the Outer Barrel (TOB). In the endcaps, there are two pixel layers and three inner disk (TID) and nine outer forward silicon disk detectors which enable coverage up to $|\eta| = 2.5$. The layout of CMS tracking detectors is shown in Figure 2.4 (from Ref. [23]). A detailed description of the tracker design can be found in [7, 23].

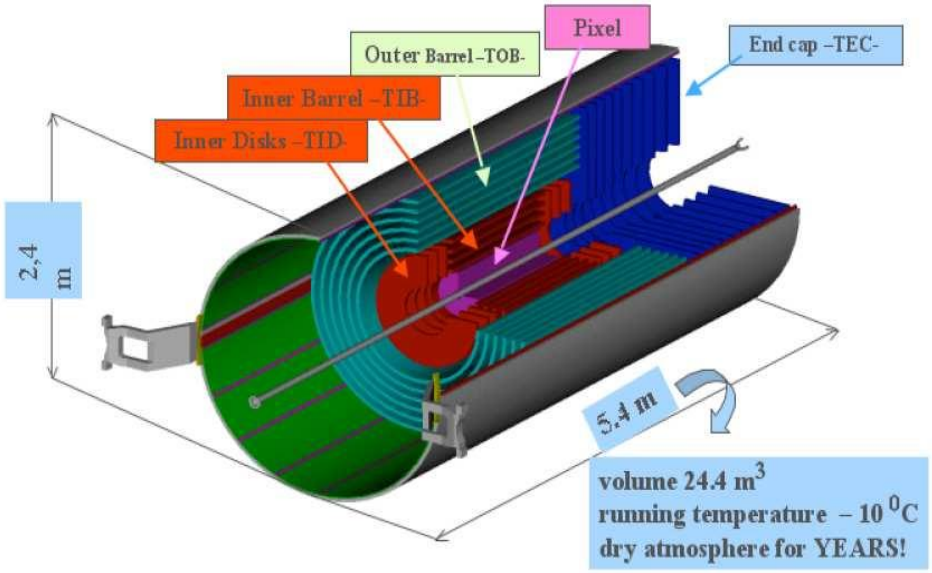

Figure 2.4: A schematic layout of the CMS tracking system.

The Pixel Tracker

The pixel tracker has two parts. The first part has three cylindrical barrel layers: 4.4 cm, 7.3 cm, and 10.2 cm from the interaction point with a length

of 53 cm. Another part has two endcap discs spreading from 6 cm to 15 cm in radius, placed on each side of the barrel at |z| = 34.5 cm and 46.5 cm. There are 66 million pixels of size $\sim 100 \times 150\,\mu\text{m}^2$ arranged across 768 and 672 modules in the barrel and endcaps, respectively. An almost square shape of the pixel is used to maximize the vertex resolution. The endcap discs are assembled with a turbine-like geometry with blades rotated by 20°. The resultant spatial resolution is 10 μm in $r-\phi$ and 20 μm in z, allowing a primary vertex resolution of $\sim$40 μm in z.

The Strip Tracker

The strip tracker is attached on the outside of the pixel detector. The basic unit of this sub-detector is called a module, each housing 512 or 768 strips. The silicon strip tracker is composed of almost 15,400 modules. They are mounted on carbon fiber structures inside a cold outer support tube with an operational temperature of $\sim$ 20 °C. In this tracker, 9.6 million microstrips are arranged in six regions: the Tracker Inner Barrel (TIB), two Tracker Inner Disks (TID), the Tracker Outer Barrel (TOB) and two Tracker Endcaps (TEC). The silicon strip length is 11.9 cm for radii $<$ 59 cm and 18.9 cm for the remaining. The longer detectors are thicker (500 μm) than the shorter ones (320 μm) to maintain a constant signal/noise. Barrel and endcap strips lie along the z and radial directions, allowing precise measurement of the r and ϕ and the z and ϕ coordinates,

respectively. To improve the track resolution, some double-sided modules are also used. Each of them consists of a regular module and a stereo counterpart angled at 100 mrad back-to-back. They provide a three-dimensional hit measurements in r, ϕ, and z. This layout allows the tracker to provide 8 to 14 hit measurements for high momentum tracks and up to $|\eta| < 2.4$.

2.2.2 The Calorimeter

Electrons, photons, and hadrons are stopped by the calorimeters allowing their energy to be measured. The first calorimeter layer is designed to measure the energies of electrons and photons with high precision. Strongly-interacting particles, i.e. hadrons, deposit most of their energy in the second layer, called the hadron calorimeter. Muons deposit only a very small fraction of their energy in the calorimeters, and they are detected with tracker and muon detector subsystems.

The Electromagnetic Calorimeter

The electromagnetic calorimeter (ECAL), which has been designed to measure electromagnetically interacting particles, photons and electrons, with high precision, is a hermetic and homogeneous detector. The ECAL is a scintillating detector in which scintillation light is emitted with a time scale on the order of the LHC bunch crossing time (25 ns).

The Hadronic Calorimeter

The CMS hadronic calorimeter (HCAL) is located behind ECAL. It is divided into the HCAL barrel (HB) and HCAL endcap (HE) subdetectors. It is designed to detect jets and measure their energies. It also complements identification of electrons, muons, and photons. Besides that, it plays an important role in the identification of neutrinos by measuring the balance of deposited transverse energy and determining missing transverse energy. The energy measurement is made through ionization which is converted to an electrical signal which is then digitized.

2.2.3 The Magnet

The central feature of the CMS apparatus is a superconducting solenoid of 6 m internal diameter, 13 m length. The large superconducting solenoid generates a uniform 4 Tesla magnetic field, required to achieve a muon momentum resolution of $\sim 10\%$ at a momentum of 1 TeV/c. It is designed to provide information on particle momenta from the bending of their tracks. Except for the outer hadron calorimeter, the calorimeters and the tracking detectors are situated within this coil to minimize energy resolution loss as the particles pass through. The iron yoke interspersed with muon chambers, returns the magnetic flux. Details on the CMS magnet can be found in [7, 24].

2.2.4 The Muon System

The CMS muon system is the muon tracking device situated in the outermost region of the CMS detector. The muon system combined with the tracker identifies muons with high efficiency and with good momentum resolution within $|\eta| < 2.4$.

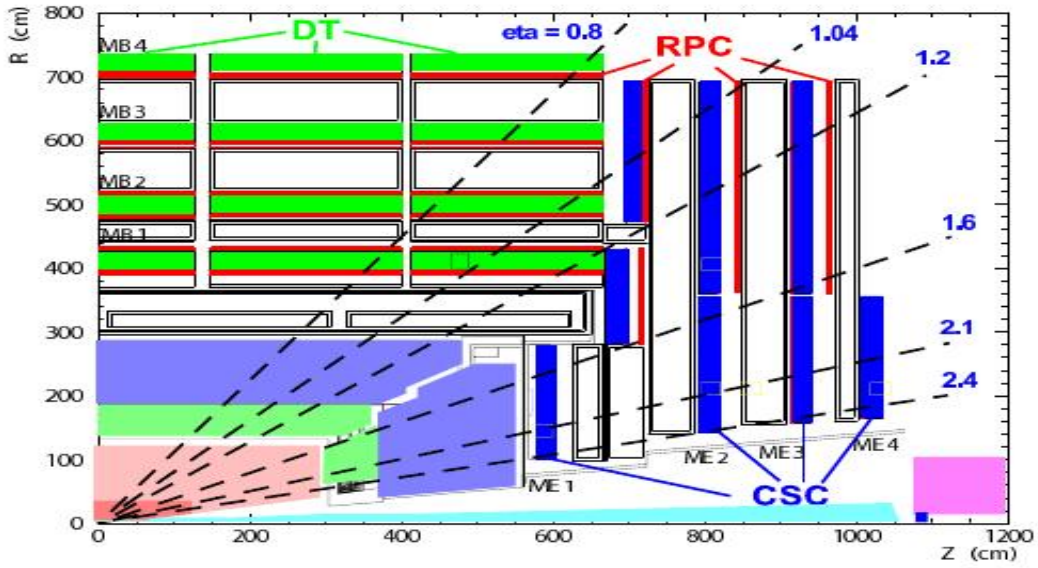

Figure 2.5: A schematic view of one quadrant of the muon system.

The muon system employes three different types of detectors. Drift tubes (DT) in the barrel are located within $|\eta| < 1.2$, cathode strip chambers (CSC) are in the endcaps for $0.9 < |\eta| < 2.4$, both are assisted by resistive plate chambers (RPC) throughout barrel and endcap in $0 < |\eta| < 1.6$. The CSC system consists of 468 chambers mounted on the endcap disks (YE±1, YE±2, and YE±3), perpendicular to the beam pipe, and arranged in four layers, called

muon endcap (ME) stations, in each endcap. Figure 2.5 (from Ref. [16]) shows the muon stations for one quadrant of the CMS detector.

The DT system comprises 250 chambers mounted onto the five wheels (YB0, YB±1, and YB±2) of the barrel yoke and arranged into four concentric layers, called muon barrel (MB) stations, interleaved with the steel yoke plates. DTs assembled in chambers containing twelve layers of tubes are aluminum tubes with a stainless steel wire in the middle. Every chamber has twelve planes of DT's which are organized in three independent sub-units made up of four planes with parallel wires. Two sub-units measure the coordinate in the bending plane and the third measures the track coordinate along the beam. Measurements in a chamber are combined to form an oriented segment, which is used for track reconstruction.

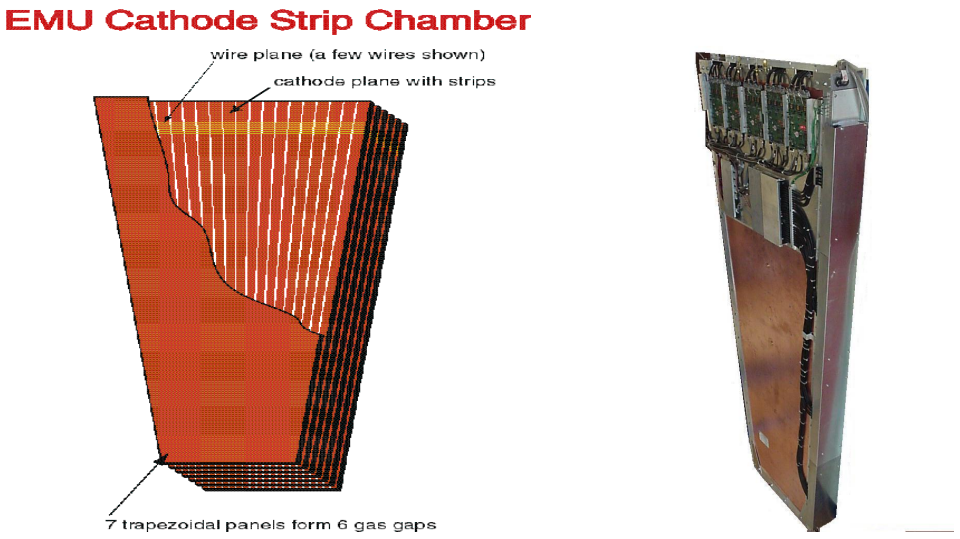

Figure 2.6: Cathode Strip Chamber.

CSCs are multiwire proportional chambers where the cathode is subdivided into strips perpendicular to the anode wires as shown in Figure 2.6 (from Ref. [25]). RPCs are used in both the barrel and the endcaps.

Muon Alignment

In order to determine the positions and orientations of the muon chambers accurately, the CMS alignment strategy combines precise survey and photogrammetry information, measurements from an optical-based muon alignment system, and the results of alignment procedures based on muon tracks. The DT and CSC detectors are used to obtain a precise position measurement. The DT layers provide a spatial resolution of 100 μm [28]. The CSCs provide 80-450 μm depending on the station [28].

With the exception of the central wheel, which is fixed, the other wheels and disks are movable along the beam direction to allow opening the yoke for the installation and maintenance of the detectors. Gravitational distortions lead to static deformations of the yoke elements that generate displacements of the muon chambers with respect to their design position of up to several millimeters. These displacements can be measured within a few hundred microns by photogrammetry when the detector is open. It is explicitly assumed that the reconstruction of CSC positions at B = 3.8 T has very similar errors as the B = 0 T reconstruction, because the same reconstruction method is applied in

both cases. The positions of each disk at various locations are surveyed when the disks are open and they are also surveyed during closing of the disks. Similarly, CSC chambers can be located by photogrammetry to a few hundred microns within the disks in the plane perpendicular to the beam line. However, the repositioning of the large elements of the yoke after opening and closing of the CMS detector, though rather precise, cannot be better than a few millimeters given their size and weight. In addition, the magnetic flux induces huge forces that cause deformations and movements that may be as large as several millimeters, and these must be carefully tracked by the alignment system. The eleven yoke elements are compressed and slightly tilted. The endcap disks are bent and the central part of the YE$\pm$1 disks is deflected inward by roughly 15 mm. Thermal equilibrium of the yoke is reached after several months of operation, with thermal effects expected in the sub-millimeter range. All these displacements and deformations are either partially or totally non-reproducible, and their typical size is an order of magnitude larger than the desired chamber position accuracy.

The CMS alignment system consists of four independent parts: the internal alignment of the tracker, DT, CSC systems, and the Link system. The muon alignment system is designed to provide continuous monitoring of the muon chamber positions in the entire magnetic field range between 0 T and 4 T, and to meet the challenging constraints of large radiation and magnetic field tolerance, wide dynamic range, high precision, and tight spatial confinement. The system

is based on a number of precise rigid structures independently supported by the tracker and by each yoke element. These structures contain optical sensors that look at the relative positions of chambers within the same yoke element. The connection among the structures located on the various yoke elements is possible only when CMS is closed, and is obtained through a network of laser beams, local distance sensors, and digital cameras.

The CMS collaboration conducted a month-long data-taking exercise known as the Cosmic Run At Four Tesla (CRAFT) for the first time during October and November of 2008, with the goal of commissioning the experiment for extended operation [26]. With all installed detector systems participating, CMS recorded 270 million cosmic-ray muon triggered events with the solenoid at its nominal axial field strength of 3.8 T in 2008. A high operational efficiency was achieved. Above 98% of optical sensors were operational for the whole system. The knowledge of detector conditions, such as the magnetic field, is of particular importance for the alignment system.

The internal alignment of tracker elements is described elsewhere [27]. The muon barrel alignment system measures the positions of the DT chambers with respect to each other and to the entire muon barrel. Further details about the barrel alignment, link alignment, and their results beyond the scope of this dissertation can be found in [28]. The muon endcap alignment system is explained in Chapter 3.

Data Acquisition

The muon alignment data acquisition system is independent of the CMS event flow. Each alignment subsystem consists of entirely different types of sensors and electronics. The time required to record a complete set of data for each subsystem is $\approx$ 18 minutes for the endcap, $\approx$ 27 minutes for the link, and $\approx$ 2 hours for the barrel. The data acquisition program is fully integrated into the CMS detector control system.

Offline Muon Geometry Reconstruction

The muon alignment system uses a dedicated reconstruction program called CMS Object-oriented Code for Optical Alignment (COCOA) [29, 30, 31] to transform the various measurements into a reconstructed DT and CSC aligned geometry. These codes have been validated using simulated and real measurements for the muon alignment system. The software reconstructs the position and orientation of the optical system objects and chambers, and performs a full propagation of errors to take into account the correlations between different measurements. For the entire muon alignment system, COCOA works with about 30,000 parameters: $\approx 3,000$ for the link, $\approx 6,500$ for the endcap, and $\approx 20,000$ for the barrel. The alignment geometry of the chambers and all alignment objects within the system are organized in a hierarchical order using a system description which must be provided in addition to the measure-

ments themselves. This description includes the interconnection of elements, e.g., laser-sensor association, and the system hierarchy, e.g., system elements association to mechanical structures, together with an approximation of the geometry obtained from other measurements (calibrations or photogrammetry). The output of COCOA contains the best geometrical description of the system compatible with the measurements and with the information from structure calibrations. Propagated uncertainties for all aligned objects are also provided.

2.2.5 The CMS Trigger and Data Acquisition

The CMS trigger decides in real-time which subset of data is to be read out by the detector and archived for offline analysis. The data acquisition (DAQ) system collects the data from the different parts of the detector, converts the data into a suitable format and saves it to permanent storage. Figure 2.7 shows schematic view of the CMS trigger and DAQ. Bunch crossings occur at LHC every 25 ns. The CMS produces about 1 MB of data at each crossing, which can not be handled by current storage and network solutions. Hence, a trigger and data acquisition (DAQ) system is required to select the interactions containing physics processes of interest with a rejection factor of $\sim 10^6$. At CMS, the events are filtered in two stages; using Level-1 (L1) trigger and High-Level Trigger (HLT).

The L1 trigger uses the calorimeter, muon system, and global triggers,

that combine the data from calorimeters and the muon system. The "trigger-primitive" primary objects (photons, electrons, muons, and jets) are reconstructed using the detector systems. These objects are created only if the p_T or E_T are above some thresholds. The L1 trigger decides in 3.2 μs to store or not to store an event and reduces the event rate from 40 MHz bunch crossing frequency to 100 kHz for further rejection by the HLT.

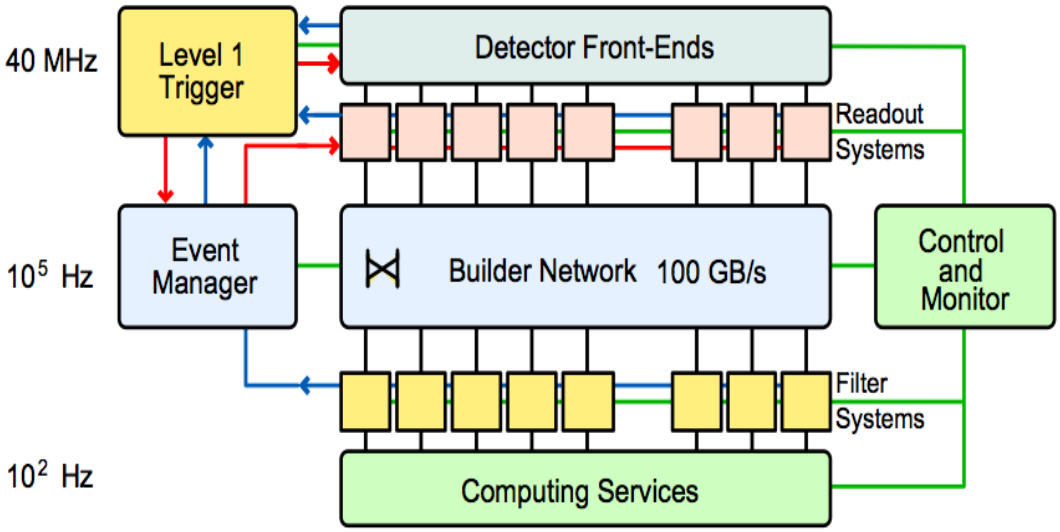

Figure 2.7: Trigger and DAQ scheme of CMS

The HLT first partially reconstructs events using the calorimeters and the muon system. At this stage, it refines the objects passed from L1. Then, it combines the data from tracker for further rejection. HLT reduces the 100 kHz L1 event rate to $\sim$ 100 Hz.

Chapter 3

Muon Endcap Alignment

3.1 Introduction

The muon endcap alignment system monitors the positions of a subset of the 468 Cathode Strip Chambers (CSCs) with sizes up to 3.4 m $\times$ 1.5 m in the two muon endcaps. Figure 3.1 shows an overview of components in the muon endcap alignment system as implemented in a simulation of the system geometry. The system uses transverse laser lines across the face of each yoke disk to measure the deflection in z_{CMS} and longitudinal laser lines to measure the rotation of each yoke disk. Each muon endcap station is monitored through three radial straight line monitors running along the full diameter of the supporting disks. Each straight line monitor consists of laser beams detected by two optical sensors in each of the four crossed chambers. Approximately one sixth of the CSC

chambers are directly monitored; the rest are aligned with respect to these monitored chambers by detecting tracks that pass through their overlapping regions.

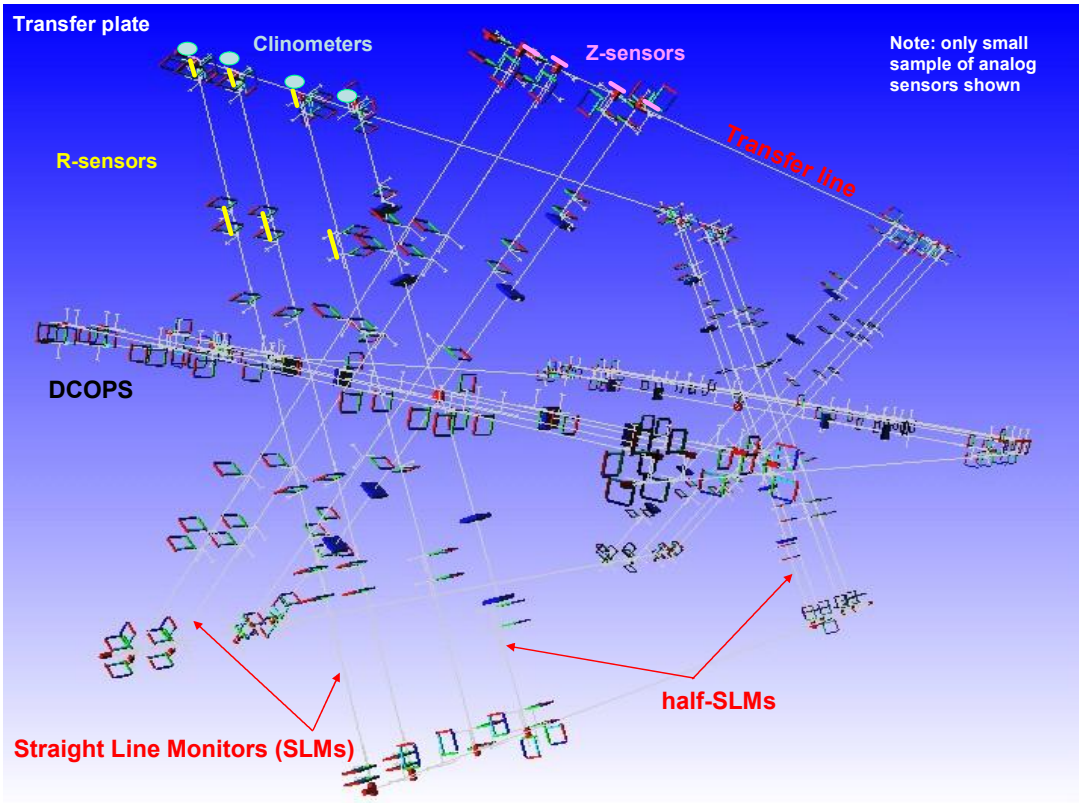

Figure 3.1: Optical components of the entire CMS muon endcap alignment system. The square objects represent digital CCD based optical position sensors (DCOPS) for monitoring three straight laser lines across each muon endcap station.

3.2 Muon Endcap System Layout and Geometry Reconstruction

A complex arrangement of five types of position sensors, as shown in Figure 3.1, measures the global r_{CMS}, ϕ_{CMS}, and z_{CMS} coordinates of one-sixth of all CSC chambers. Unmonitored CSC chambers can be coarsely aligned with the average displacements and rotations observed for monitored chambers in the corresponding rings. This allows adequate monitoring of the yoke disk deformations due to strong magnetic forces. All CSC alignments are subsequently refined with tracks that traverse overlapping chambers. For the ME1/3 chambers, which do not overlap, azimuthal distances between the chambers are additionally monitored by proximity sensors.

Details on the performance requirements and the design of the system and its sensors can be found in our publications [25, 32]. Here we briefly mention the main features of the system used in this analysis. The Muon Endcap alignment system is required to monitor chamber positions with 75-200 μm accuracy in the $r\phi$ plane, 400 μm in the radial direction, and 1 mm in the z-direction along the beam axis [32]. Three straight-line monitors (SLMs) within the $r\phi$ plane of each muon endcap station, as shown in Figure 3.2, measure global z_{CMS} and ϕ_{CMS} chamber positions relative to references located at the outer edges of the stations.

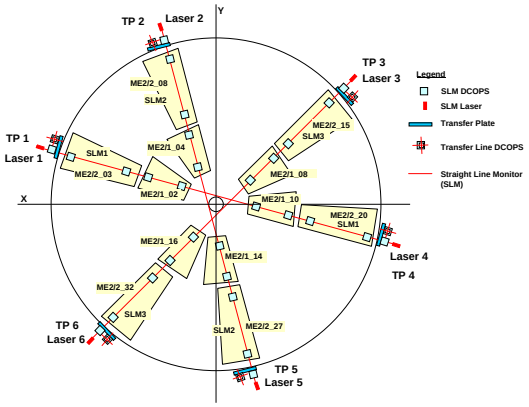

Figure 3.2: Schematic $r\phi$ view of straight-line monitors in the ME2 station. Locations of axial transfer lines running perpendicular to the plane and across endcaps are indicated. Optical sensors and other alignment components are also shown.

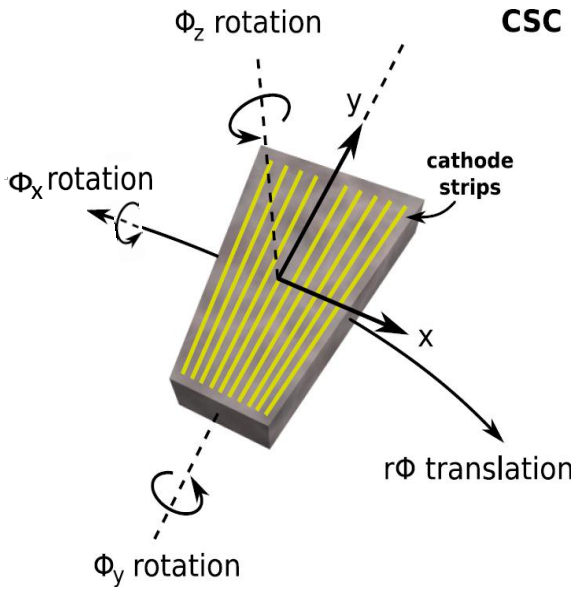

Figure 3.3: Local coordinates and alignment parameters of a CSC chamber.

A semi-local coordinate system for the entire chamber is defined with x, y, and z axes nominally parallel to the layers' axes, but with a single origin as shown in Figure 3.3 (from Ref. [27]). The nominal x direction of every chamber is perpendicular to the beamline and radial projections from the beamline. An SLM measures global z_{CMS} and ϕ_{CMS} chamber positions precisely and radial sensors measure r_{CMS}. It also determines in chamber rotations $\phi_{x_{\text{local}}}$ around their local x-axes. Though the COCOA outputs the positions and orientations of chambers in six degrees of freedom, currently used measurements are only sensitive in z_{CMS}, ϕ_{CMS}, and $\phi_{x_{\text{local}}}$. At present, other degrees of freedom are used from the track-based alignment.

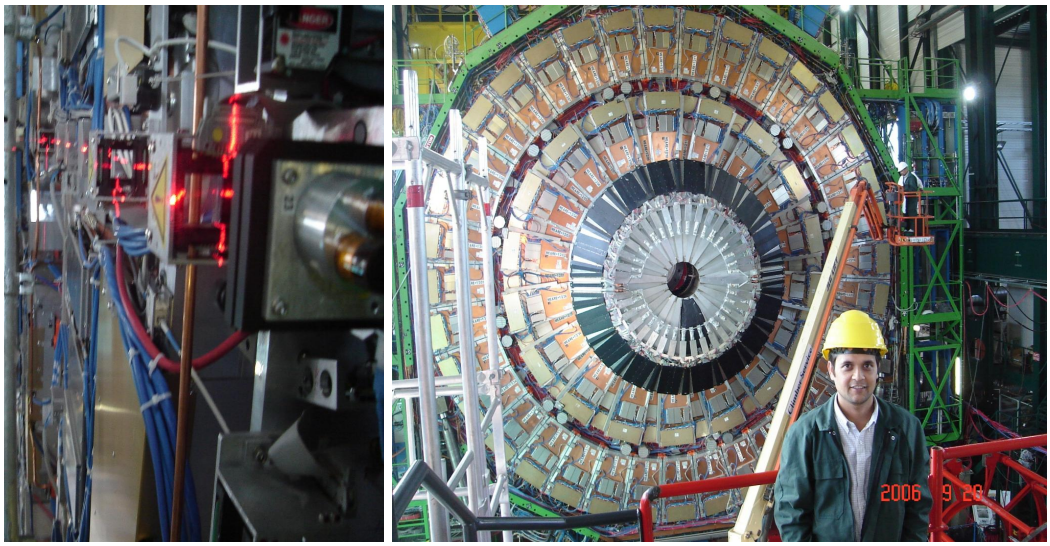

Figure 3.4: Commissioning of muon endcap system (left) and fully instrumented CMS Muon Endcap station ME+1 (right).

An SLM locates four CSCs with two Digital CCD Optical Position Sensors (DCOPS) mounted on each CSC. Two more DCOP sensors are mounted on transfer plates located at the edge of the yoke disk. Two crosshair lasers, which emit a nearly radial laser beam across four chambers from each end, provide straight reference lines that are picked up by two DCOPS on each chamber. This arrangement provides references for the chamber positions relative to the laser lines. The CCDs were illuminated separately by the lasers at each end of the SLM. Figure 3.4 (left) shows a cross-hair laser passing through the optical sensors across the muon endcap disk in an SLM. One of the muon endcap stations (ME+1) instrumented with cathode strip chambers is also shown in Figure 3.4 (right). Note the outer ring of chambers on ME+1, only where the CSCs do not overlap in ϕ.

In the ME1 stations, the straight-line monitors cannot reach across the entire endcap yoke disk as they are blocked (by design) by the endcap calorimeters attached to the YE1 yoke disks as shown in Figure 3.4 (right). Instead of three full-length straight-line monitors, there are six half-length straight-line monitors in each ME1 station. Each half straight-line monitor observes two chambers (one in the ME1/2 ring and one in the outer ME1/3 ring) and connects to the link alignment laser lines at the inner radius and to the barrel MABs at the outer radius. The geometry of the ME4 straight-line monitors is identical to those on the ME2,3 stations despite the absence of the complete outer ring of

ME4/2 chambers. This identical design is intended as a preparation for a future planned CMS upgrade that will add remaining outer ME4/2 chambers.

Optical transfer lines run parallel to the CMS z-axis along the outer cylinder envelope of CMS, at six angles separated by 60° in ϕ_{CMS}. These axial lines provide an optical connection between the forward and backward muon endcaps, across the barrel wheels. Distancemeters, mounted around the periphery of each ME station, measure the z_{CMS} location of the outer edge of the ME stations relative to the external MAB positions on the YB2 wheels.

3.3 Reconstruction of CSC Positions

The analysis of CRAFT data focuses on determining CSC positions in global z_{CMS} and rotations $\phi_{x_{\text{local}}}$ around their local x-axes. This complements track-based alignment, which is mainly suitable for alignment in the $(r\phi)_{CMS}$ plane [27].

To reconstruct the chamber positions, the COCOA model of the system is required. The model for the entire muon endcap station has been developed using the drawings of individual components and an outline of an old scheme [34] for the endcap alignment system. The reconstructed positions of each components of the system in the hierarchy were obtained using ideal measurements of the sensors and compared with ideal positions. We found a discrepancy of ~ 2 mm in radius with the official record for the ideal positions of chambers for

outer rings on ME2,3,4. After our findings of correct geometry using COCOA, the official record for the ideal positions of those chambers has been corrected. With this model, the necessary adjustments (e.g. shimming) were implemented to reconstruct the positions using the alignment data at 0T with the validation.

3.3.1 Chamber Positions in Stations ME2,3,4 Measured with Straight-Line Monitors

The geometry reconstruction starts by performing the basic alignment procedure described in Section 3.2. Measurements taken at B = 0 T are used for the reconstruction of CSC positions. An example of such a reconstruction in z_{CMS} at B = 0 T is shown for one straight-line monitor in Figure 3.5. The discrepancies in z_{CMS} between reconstructed values and photogrammetry measurements are shown in Figure 3.6 for all ME2,3,4 stations.

First, we reconstructed chamber positions using the same transfer plate (TP) and the endcap yoke disk center positions from the survey [35] for ME2,3,4 SLM reconstruction at 0T and 3.8T and provided the muon endcap alignment constants for the first CRAFT reprocessing. The positions change with the magnetic field and are monitored with other alignment sensors as shown in Figure 3.1. In order to provide more realistic and accurate muon endcap alignment constants, measurements from Z-sensors on the transfer plates are incorporated

into the COCOA geometry model of each SLM for the determination of their instantaneous positions. The outline of the locations of Z-senors in the endcap and an actual picture of the Z sensor at point 2 of ME+2 are shown in Figure 3.7. We tried to validate the Z-sensor measurements at 0T with survey measurements for the transfer plate positions and found a discrepancy of several mm. The muon endcap system has to depend on other subsystems and they use the photogrammetry measurements or survey, so it was decided to use the relative shifts as shown in Figure 3.8 from Z-sensor measurements at 0T and 3.8T. The transfer plate position at 3.8T is updated by adding the corrsponding relative shifts from Z-sensor measurements to the TP position at 0T from the survey. One then proceeds to reconstruct the absolute z_{CMS} positions of all monitored CSC chambers at B = 3.8 T, using as input field-on sensor measurements, the absolute z_{CMS} positions of the endcap yoke disk centers provided by survey [35] that are listed in Table 3.1, and the relative z_{CMS}-displacements measured between B = 0 T and B = 3.8 T.

As an example of field-on reconstruction results, Figure 3.5 (bottom) shows the reconstruction for the straight-line monitor between transfer plates 1 and 4 in ME+3 at B = 3.8 T. Comparing this result with the reconstruction for the same straight-line monitor at B = 0 T (Figure 3.5 top) demonstrates that the endcap yoke disk bends due to magnetic forces. Analogous reconstruction plots for data taken at B = 3.8 T with the other straight-line monitors show

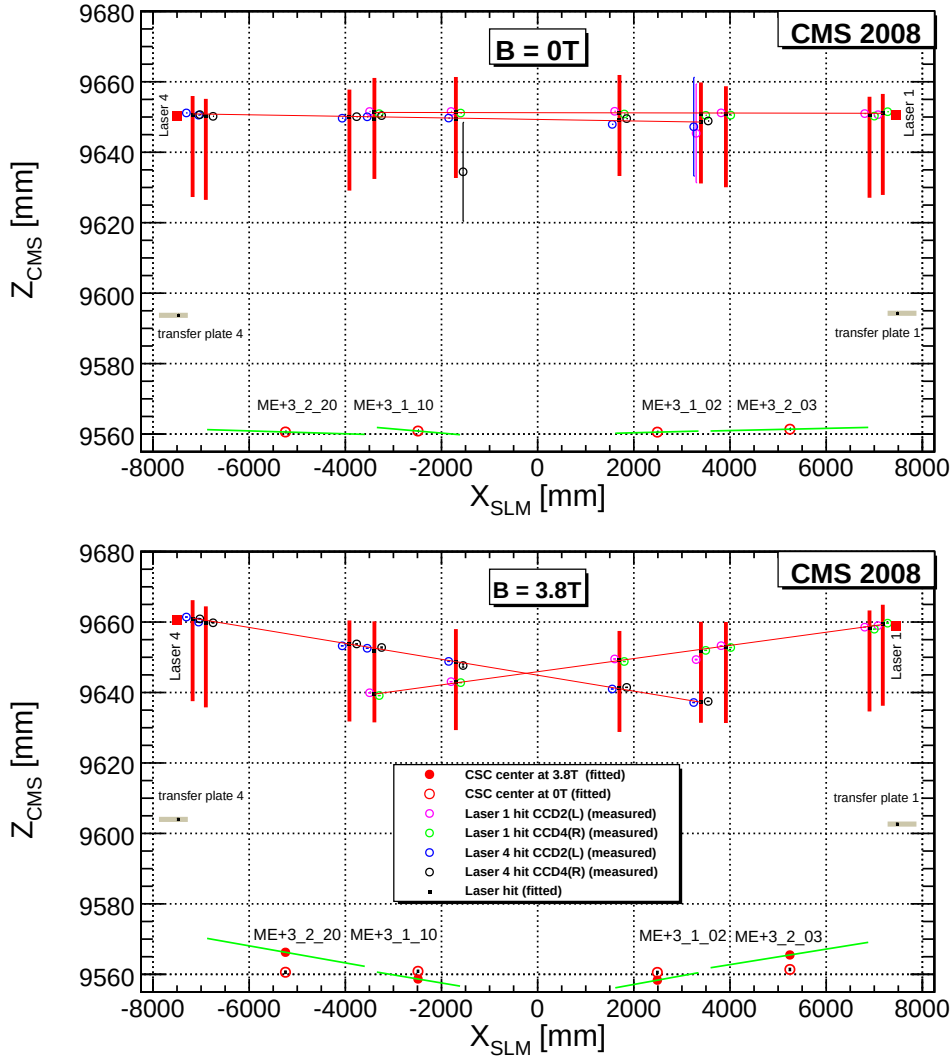

Figure 3.5: Reconstruction results for positions of chambers and sensors in z_{CMS} vs. their positions x_{SLM} along a straight-line monitor at B = 0 T (top) and 3.8 T (bottom). The data shown are for the straight-line monitor connecting transfer plates 1 and 4 of station ME+3. Large vertical bars indicate fitted positions of optical sensors. Laser hits on optical sensors are indicated by open circles with error bars on hit positions smaller than marker symbols.

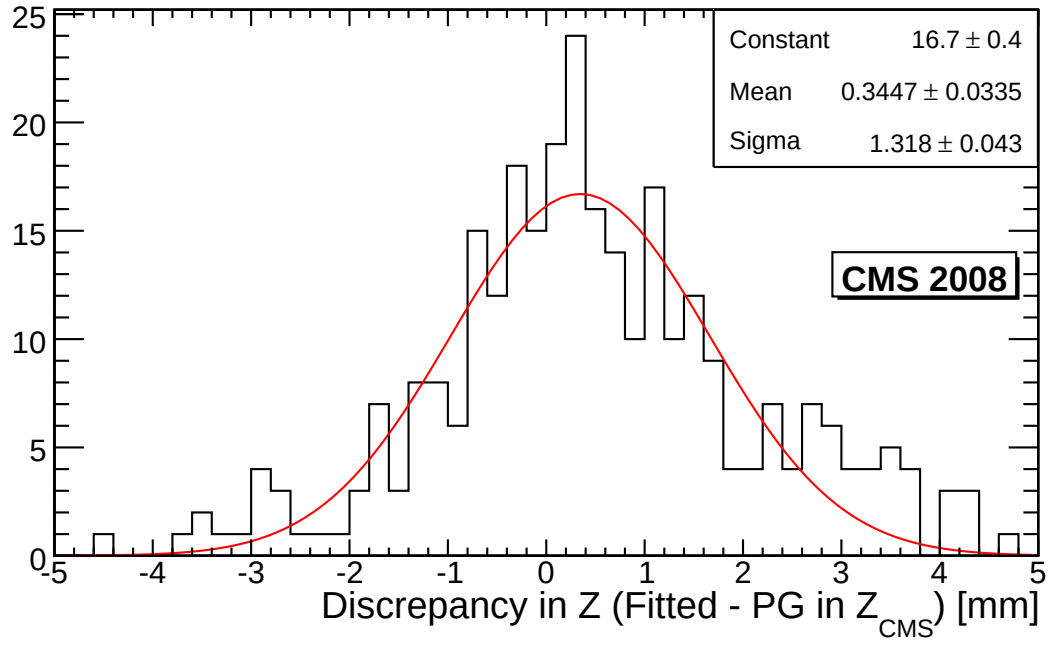

Figure 3.6: Discrepancies Δz_{CMS} between z_{CMS}-positions reconstructed by CO-COA and measured by photogrammetry (PG) at B = 0 T. For CSC centers, alignment pins, and optical sensors in ME2,3,4 stations using full straight-line monitors fitted with a Gaussian.

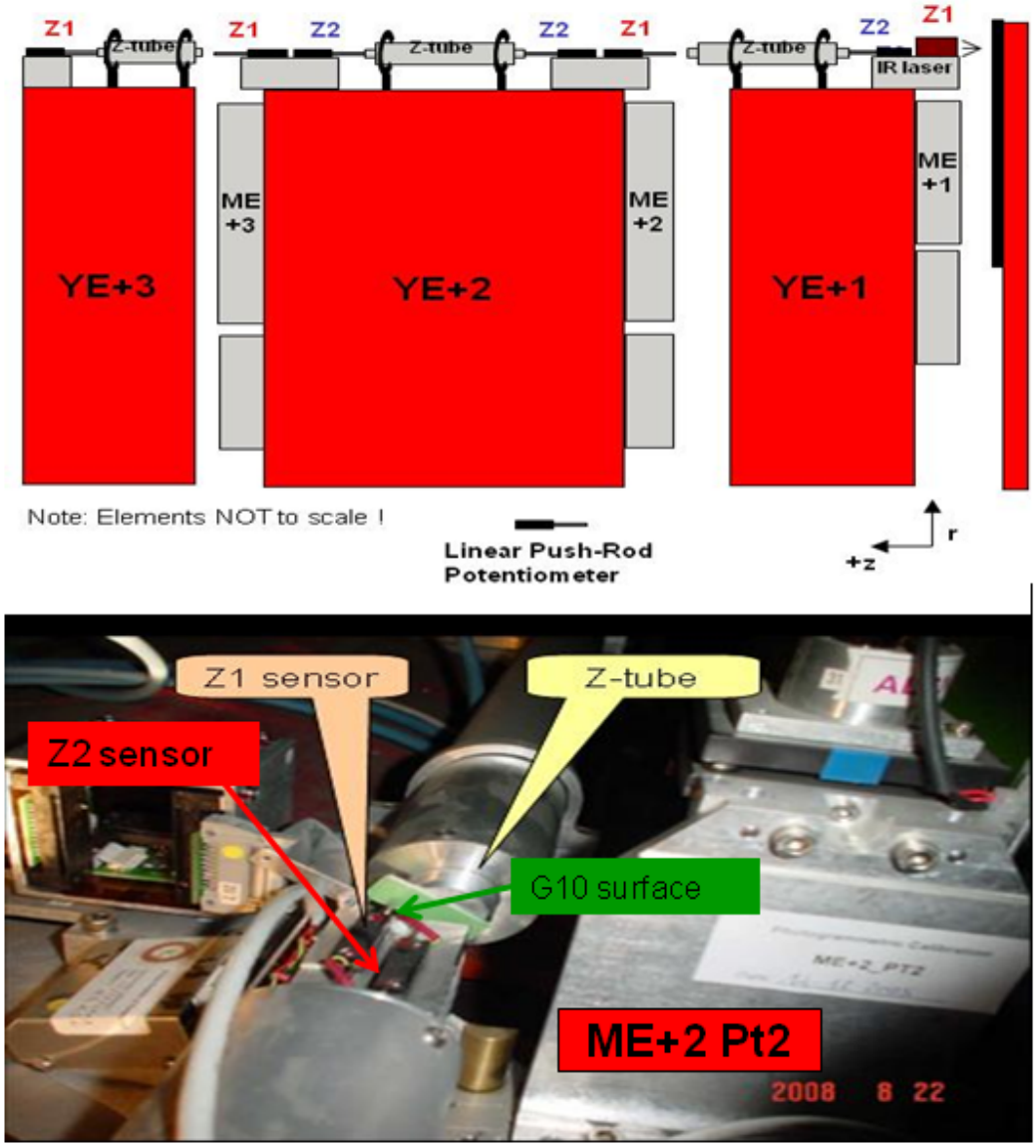

Figure 3.7: Outline of Z-sensors in the endcap (top) and an actual Z-sensor set up at the point 2 of ME+2 (bottom).

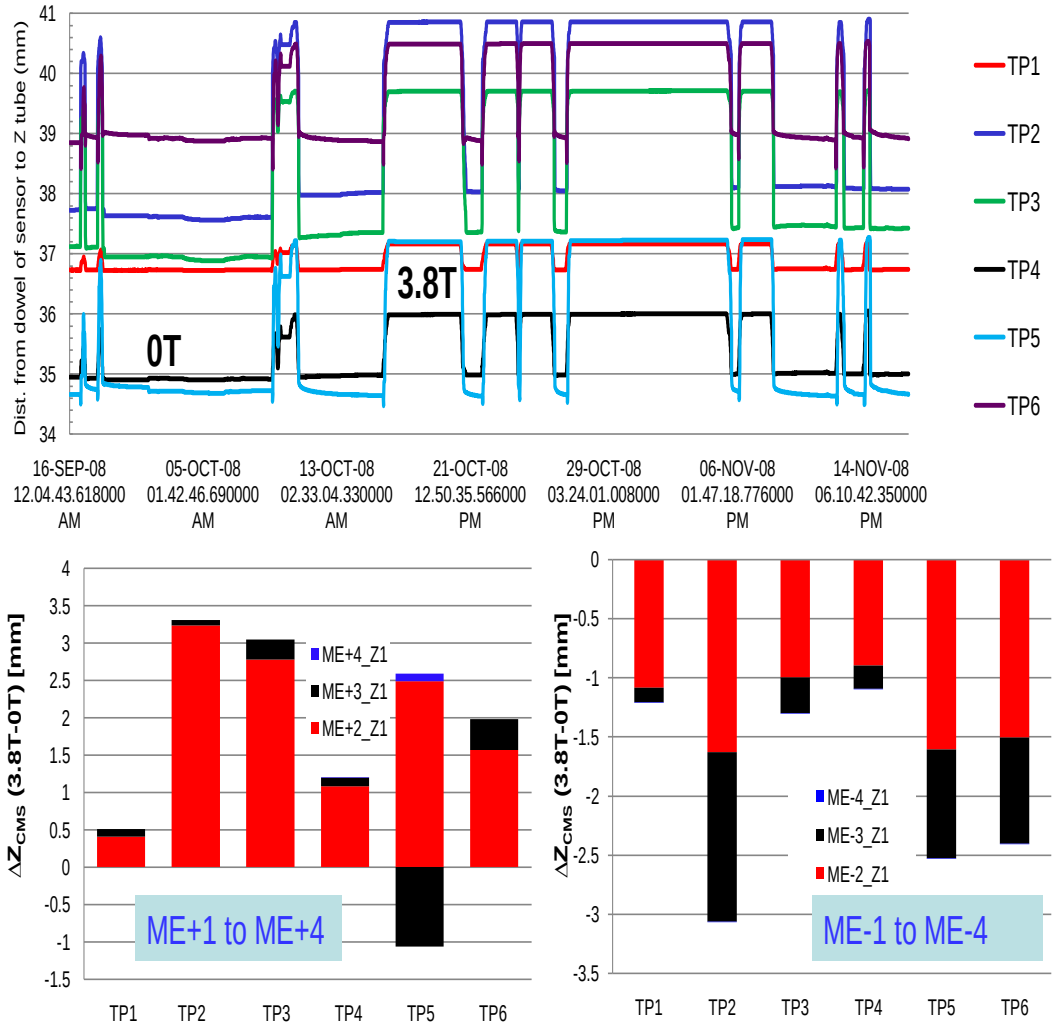

Figure 3.8: Z-sensor measurements show the instantaneous position of transfer plate with changing magnetic field (top) and the relative displacements in z_{CMS} at 3.8T and 0T from ME1 to ME4 (bottom).

Table 3.1: Positions of muon endcap yoke disk centers in global CMS coordinates, measured by survey with closed and locked detector before the start of the CRAFT test. Nominal global z-position of yoke disk centers are also shown for comparison (nominal (x,y) coordinates are (0,0) for all yoke disks. The uncertainty for all listed measurements is 0.3 mm.

Yoke disk center	x_{CMS}^{meas} [mm]	y_{CMS}^{meas} [mm]	z_{CMS}^{meas} [mm]	z_{CMS}^{nominal} [mm]
YE+3	1.6	0.6	9906.5	9900.0
YE+2	0.2	0.8	8828.3	8820.0
YE+1	1.5	−0.3	7568.2	7560.0
YE–1	2.0	−0.4	−7561.7	−7560.0
YE–2	4.1	−1.1	−8821.6	−8820.0
YE–3	−1.1	0.4	−9903.1	−9900.0

similar deformations of all yoke disks towards the interaction point by about 10 to 12 mm for the chambers on the inner rings and by about 5 mm for the chambers in the outer ring, respectively. The relative z_{CMS}-displacements for all monitored CSC chambers for the ME2,3 stations measured between B = 0 T and B = 3.8 T are shown in Figure 3.9.

We summarize our reconstruction results for the ME2,3 stations in Figure 3.10. The yoke disk deformations shown in this figure are calculated from the differences of reconstructed positions of the CSC alignment pins at B = 0 and 3.8 T. Quadratic fits describe the yoke disk deformations reasonably well. A quadratic dependence on the magnetic field is apparent, which is in agreement with expectations from Finite Element Analysis of disk deformations [9, 32]. These results are consistent with ME+2 reconstruction results using first magnet test data taken in 2006 at 4 T [25]. The differences observed by different straight-line monitors for the same station indicate a slightly asymmetric deformation of the yoke disks. Some asymmetry is expected because the endcap yoke disks are fixed at the bottom to massive carriage structures that are used to move the yoke disks as needed.

The precision of the reconstruction is estimated from COCOA's error propagation to be 280 μm and 320 μm in z_{CMS} for the inner and outer rings of chambers, respectively, and 200 μrad in $\phi_{x_{\mathrm{local}}}$. The angular uncertainty has a contribution from the error in z_{CMS} and the chamber length. Figure 3.6 shows

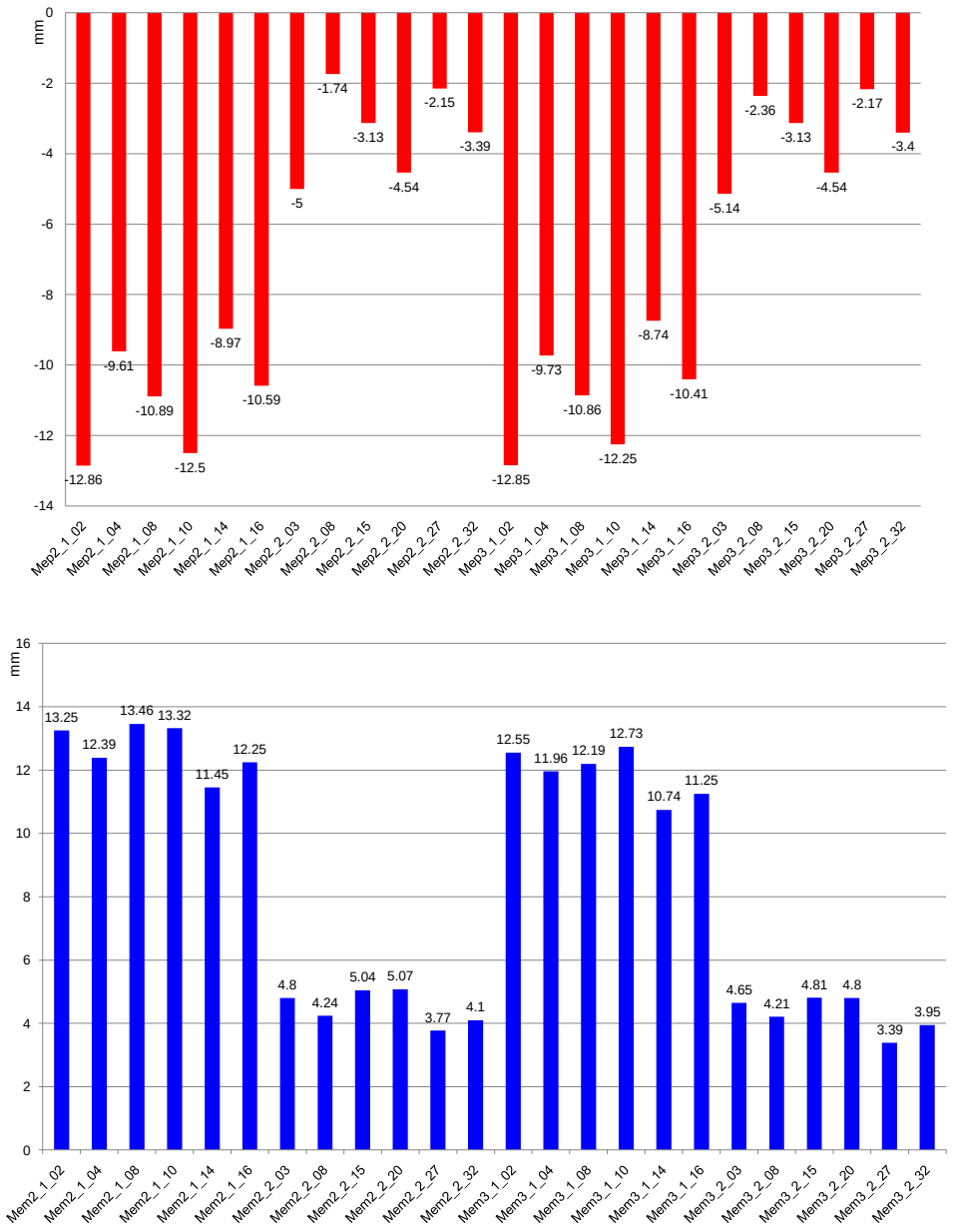

Figure 3.9: Relative displacements in z_{CMS} from reconstruction results for the position of ME+2,3 (top) and ME-2,3 (bottom) chambers at B = 0T and 3.8T. Monitored chambers are shown along the x-axis and "Mep" and "Mem" stand for ME+ and ME-, respectively.

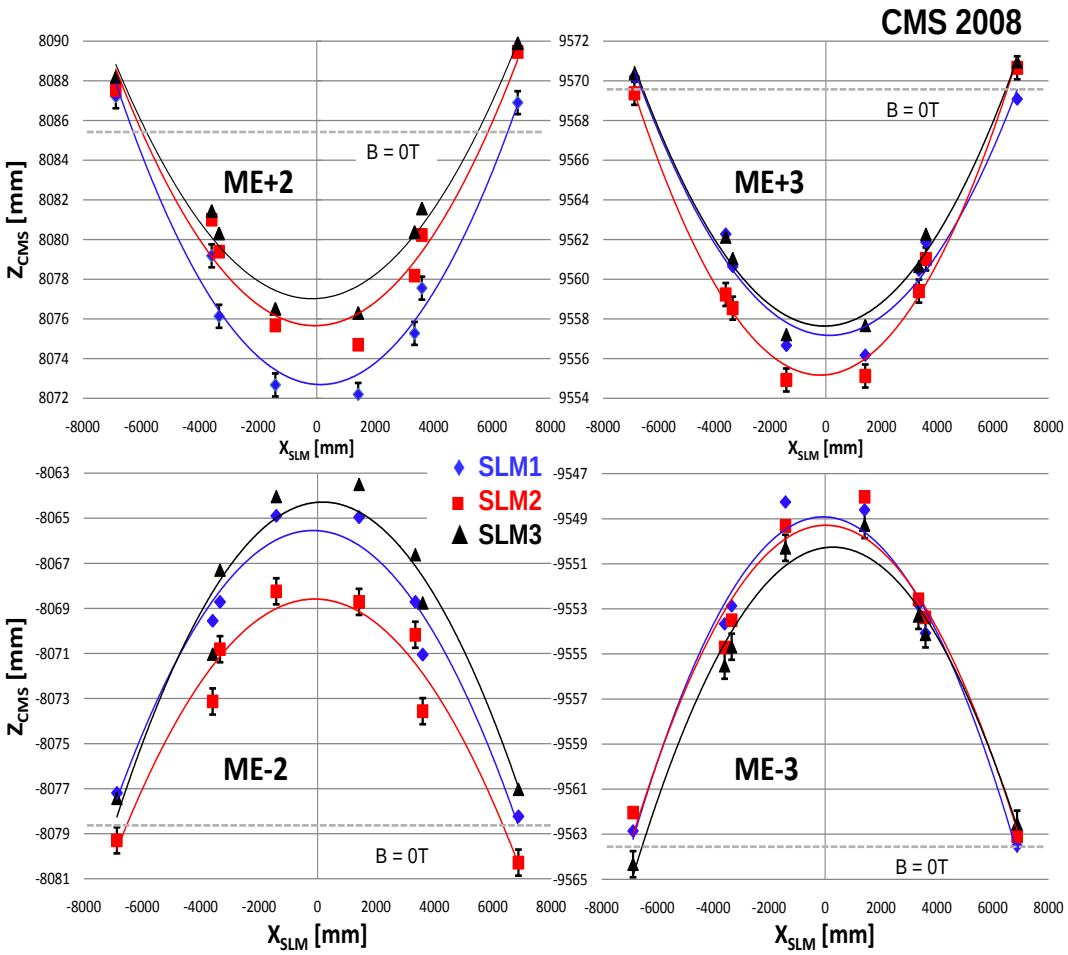

Figure 3.10: Yoke disk deformations at B = 3.8 T in ME2 and ME3 stations measured with straight-line monitors. Points shown correspond to positions of CSC alignment pins and are fitted with second order polynomials. Error bars correspond to $\sigma_{tot}(z_{CMS}) = 470\,\mu$m and apply to all measurement points. For clarity, error bars are shown only for the lowest curve in each station. Dashed lines indicate the average alignment pin positions at B = 0 T for the three SLMs in each station as measured by photogrammetry and survey.

the difference Δz_{CMS} between z_{CMS}-positions reconstructed by COCOA and measured by photogrammetry at B = 0 T for CSC centers, alignment pins, and optical sensors in ME2,3,4 stations using full straight-line monitors. We take the deviation from zero of the mean of this distribution as a measure of the systematic error of the COCOA reconstruction, i.e. $\sigma_{\text{syst}}(z_{CMS}) = 340\,\mu$m. The photogrammetry measurements used in this comparison spread over a significant time period of two years. Some measurements were done on the surface and some in the underground CMS cavern. The deviations are therefore an upper limit. Reconstruction at B = 3.8 T cannot be checked against independent survey or photogrammetry because those cannot be performed for a closed detector when the magnetic field is turned on. Consequently, we explicitly assume that the COCOA reconstruction of CSC positions at B = 3.8 T has very similar errors as the B = 0 T reconstruction, because the same reconstruction method is applied in both cases.

3.3.2 Chamber Positions in ME1

The reconstruction of CSC positions in ME1 using half straight-line monitor data is more complex than the reconstruction of full-length straight-line monitors in ME2,3,4, because additional information from the link alignment is required. We use the z_{CMS} of MABs reconstructed by the link system, together with measurements from distancemeters, to locate the ME1 yoke disk in z_{CMS}.

For the ME1/1 and ME1/2 chambers, x_{CMS}, y_{CMS}, and z_{CMS} coordinates as well as the chamber rotations ϕ_{CMS} and $\phi_{x_{\mathrm{local}}}$ around their local x-axes, are obtained from the reconstruction of the link sensors data. The reconstruction procedure and results for the chamber positions in ME1/1, ME1/2, and ME1/3 are described in Ref. [28, 36]

3.4 Muon Endcap Alignment Constants

From this study the reconstructed chamber positions at 3.8T in z_{CMS} and $\phi_{x_{\mathrm{local}}}$ are provided to the CMS in the form alignment constants, readable by the CMS software (CMSSW). For those CSC chambers that are not directly monitored by straight-line monitors, the average of the z_{CMS}-positions and $\phi_{x_{\mathrm{local}}}$-tilts obtained from the monitored chambers are used as alignment corrections in the corresponding rings. This is reasonable since we find approximate azimuthal symmetry in the yoke disk deformation (Figure 3.10). The average alignment corrections with respect to the nominal geometry are listed for each CSC ring in Table 3.2 and visualized as a sketch in Figure 3.11. Due to different initial positions of the forward and backward endcap yoke disks relative to nominal (see Table 3.1) the CSC alignment corrections to z_{CMS} with respect to *nominal* CSC positions are not symmetric between the two endcaps, even though the bending itself is similar for forward and backward muon stations. The CSC

alignment constants described here together with complementary constants for the other coordinates ($r\phi$ positions), obtained from track-based muon alignment [27], are used for the reconstruction of cosmic ray muon tracks in the CRAFT exercise [37].

Table 3.2: Average alignment corrections $\Delta z_{CMS} = z_{CMS}^{reco} - z_{CMS}^{nominal}$ to CSC chamber positions and orientations for each ring with respect to nominal. The typical precisions are described in the text. Dashes in the table indicate degrees of freedom not measured by the system.

Ring	ME+1/1	ME+1/2	ME+1/3	ME+2/1	ME+2/2	ME+3/1	ME+3/2	ME+4/1
$\boldsymbol{\Delta z_{CMS}}$ [mm]	−17.57	−5.49	−1.67	−0.97	6.74	−4.31	3.26	0.65
$\boldsymbol{\Delta\phi_{x_{\rm local}}}$ [mrad]	–	−4.4	−1.3	−1.9	−2.4	2.2	2.6	2.7
Ring	ME–1/1	ME–1/2	ME–1/3	ME–2/1	ME–2/2	ME–3/1	ME–3/2	ME–4/1
$\boldsymbol{\Delta z_{CMS}}$ [mm]	16.73	5.94	2.12	10.23	2.74	11.39	3.86	8.49
$\boldsymbol{\Delta\phi_{x_{\rm local}}}$ [mrad]	–	−4.4	−1.3	−1.6	−2.2	2.5	2.7	1.6

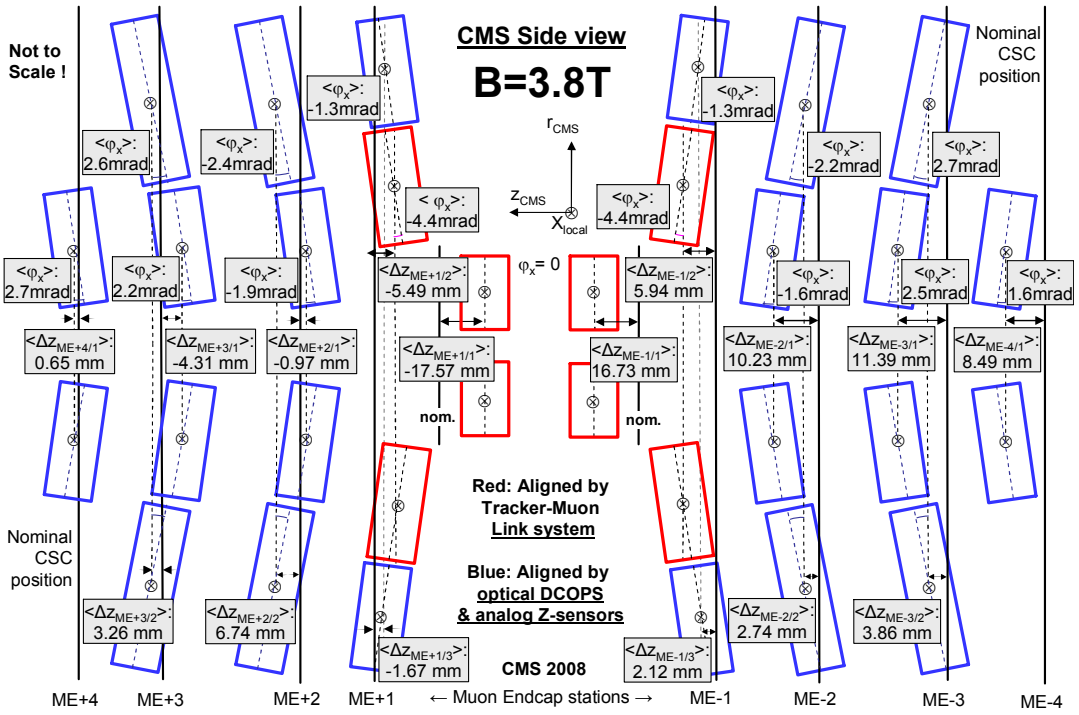

Figure 3.11: Summary sketch of average deformations and displacements from nominal positions for muon endcap stations at B = 3.8 T during CRAFT exercise, as observed with the muon alignment system. The shown displacements Δz_{CMS} and rotations $\phi_{x_{\mathrm{local}}}$ are averages over the six monitored CSC chambers in each ring.

3.5 Summary

The muon endcap alignment system successfully recorded data during the CRAFT 2008 exercise. The results obtained show several improvements as well as some shortcomings which are being or have already been addressed. The system is able to track detector movements and deformations under magnetic forces, and to monitor the stability of the detector during operation. Results are in agreement with other subsystems and with photogrammetry measurements, where these apply.

Table 3.3: Typical precisions obtained for CSC chamber alignment. A dash in the table indicates the degree of freedom not measured by the system.

Chamber	z_{CMS} [μm]	$\phi_{x_{\mathrm{local}}}$ [μrad]
CSC ME1	220–340	–
CSC ME2,3,4	280–320	200

All monitored CSC chambers were aligned in z_{CMS} and $\phi_{x_{\mathrm{local}}}$, with the exception of the ME1/1 chambers, which were aligned only in z_{CMS}. An aligned detector geometry at B = 3.8 T is provided in the form of alignment constants which are used for muon track reconstruction. The precision for ME2, ME3, and ME4 chambers ranges between 280 and 320 μm in z_{CMS}, and is approximately 200 μrad in $\phi_{x_{\mathrm{local}}}$. For the ME1 chambers, the precision in z_{CMS} ranges between

220 and 340 μm from the inner to outer rings. The systematic error associated with the reconstruction is estimated to be below 500 μm from comparison with photogrammetry. The error is within the required design accuracy of 1 mm. So, the results are acceptable.

Alignment precisions are summarized in Table 3.3. The muon alignment system was partly commissioned during CRAFT 2008. Even if a complete muon alignment reconstruction was not ready, it proved its capability to provide muon alignment with a precision close to that required by CMS. These results are quite good and acceptable.

Chapter 4

Muon Misalignments and Z' Search

4.1 Introduction

In this chapter, we study the transverse momentum (p_T) resolution for muons and the dimuon mass resolution for $Z' \to \mu^+\mu^-$ [5] (spin 1) decays and Drell-Yan events using simulated events of proton-proton (pp) collisions at $\sqrt{s} = 7$ TeV with the CMS experiment. The transverse momentum (p_T) resolution for muons from the Z' decay is studied at different masses and center-of-mass energies using different alignment scenarios. We also discuss the expected effect of systematic muon misalignments on the transverse momentum (p_T) resolution for muons from the Z' decay.

We reconstruct the high-mass dimuon samples with different muon alignment scenarios using three standard muon and tracker alignment scenarios, available in the form of global tags [38]. More information about the alignment constants for startup and $50\,pb^{-1}$ alignment scenarios can be found elsewhere [39, 40]. The most relevant items for the muon alignment scenarios and the corresponding global tag used in this study are briefly mentioned here:

- **Ideal** (MC_31X_V5): corresponding to ideal geometry of the detector
- **Startup** (STARTUP31X_V4): based on CRAFT 2008 and 2009 data analysis for early phase and produced by randomly misaligning chambers with an RMS consistent with cross-checks in the CRAFT 2009

Uncertainty in CSC chamber positions taken into account

1. 0.0092 cm layer x misalignments observed with beam-halo tracks
2. isotropic photogrammetry uncertainty of 0.03 cm (x, y, z) and 0.00015 rad in ϕ_z
3. 0.0023 rad ϕ_y misalignment observed with beam-halo tracks
4. 0.1438 cm z and 0.00057 rad ϕ_x uncertainties between rings from Hardware Straight Line Monitors (from comparison with photogrammetry in 0T data)
5. 0.05 cm (x, y, z) ME disk misalignments and 0.0001 rad rotation

around beamline

Uncertainty in DT chamber positions taken into account

1. Positions within sectors:

   For aligned chambers (wheels -1, 0, +1 except sectors 1 and 7):

   (0.08 cm, 0.1 cm , 0.1 cm) in (x, y, z) and

   (0.0007 rad, 0.0007 rad , 0.0003 rad) in (ϕ_x, ϕ_y, ϕ_z)

   For unaligned chambers

   (0.08 cm, 0.24 cm , 0.42 cm) in (x,y,z) and

   (0.0016 rad, 0.0021 rad , 0.0010 rad) in (ϕ_x, ϕ_y, ϕ_z)

2. Positions of the sector-groups:

   For aligned chambers: 0.05 cm in x

   For unaligned chambers 0.65 cm in x

3. Superlayer z uncertainty is 0.054 cm.

- **50 pb^{-1}** (50PBMU31X_V1): Assuming an alignment with tracks using $50\,pb^{-1}$ data and produced by running the Reference-Target algorithm [27] on appropriate MC samples.

  In this scenario, the starting misalignments are (0.2 cm in x, 0.4 cm in y and z, 0.002 rad in ϕ_x, ϕ_y, ϕ_z random Gaussians) in the barrel, and the startup scenarios in the endcap. The first pass of alignment is performed

with simulated cosmics. Then, the second and final pass of alignment is performed with simulated collision muons by allowing the following parameters to float:

1. DT stations 1-3: x, y, ϕ_x, ϕ_y, ϕ_z (inherit z from cosmics alignment)
2. DT station 4: x, ϕ_y, ϕ_z (others are still misaligned)
3. CSCs: x, ϕ_y, ϕ_z (inherit z and ϕ_x from hardware)

In the final result [41], this procedure yields the following uncertainties:

1. 0.04894 cm in x: all aligned chambers (everything but ME1/3 and one fit failure: ME-1/4, 8)
2. 0.09552 cm in y: wheels -1, 0, 1, stations 1-3 (only showing the ones with a reliable z alignment from cosmic rays)
3. 0.1826 cm in z: same as in y
4. 0.000366 rad in ϕ_x: DT stations 1-3
5. 0.000266 rad in ϕ_y: all aligned chambers
6. 0.0005976 rad in ϕ_z: all aligned chambers

The remaining parameters are similar to the startup scenario.

Tracker misalignment scenarios [42] in startup and 50 pb^{-1} alignments are the same and based on CRAFT 2008. The scenario describing the misalignment

of the tracker at the CMS startup (also known as "TrackerCRAFTScenario" with the tag TrackerCRAFTScenario310_mc) consists of segments of already existing scenarios for each of the tracker subdetector based on the distributions of residuals observed after the alignment of the Tracker with the data from CRAFT 2008 (about 4 million cosmic tracks).

Misalignments of the tracker and of the muon system in the early stages of collision data taking have been taken into account by using the so-called "startup" and "50 pb^{-1}" misalignment scenarios, which give estimates of the alignment achieved at startup and with an integrated luminosity of $50\,pb^{-1}$, respectively. In order to study the effect of systematic misalignment in the muon endcap system on the muon p_T resolution, we reconstruct the 1.2 TeV/c^2 and 2.0 TeV/c^2 Z' samples with the above mentioned misalignment scenarios and re-run the standard Zprime2muAnalysis [43] package, in particular the Zprime2muResolution code over the resulting simulated data sets. These muon misalignment scenarios are simulated separately with respect to ideal and startup scenarios. Since the startup alignment scenario is already biased, we use the ideal alignment scenario as well. To simulate a misaligned muon endcap system, individual muon endcap yoke disks (stations) and entire endcaps are misaligned in position (x_{CMS}, y_{CMS}, z_{CMS}) up to $\pm\,2\,$mm or rotated around the beam line, i.e. rotation angle $\phi_{z_{CMS}}$ up to $\pm\,0.5\,$mrad with steps of 0.1 mm or 0.1 mrad, respectively.

The observability of the $Z' \rightarrow \mu^+\mu^-$ channel with the CMS experiment has been studied previously [44, 45, 46] at $\sqrt{s} = 14$ TeV and also at $\sqrt{s} = 6$ and 10 TeV [47]. In this study, we update the potential of the CMS experiment to discover an additional heavy neutral gauge boson Z' in proton-proton (pp) collisions at $\sqrt{s} = 7$ TeV using Monte Carlo samples for this center-of mass energy. Finally, we present our studies of how muon misalignments could effect the signal significance.

4.2 Monte Carlo Samples

All signal and background samples used in this study are generated with PYTHIA [48] version 6.4 (with photon emission off incoming or outgoing quarks and leptons switched on) and the CTEQ6L set of parton distribution functions (PDF) [49] from LHAPDF [50] version 5.6.0. From a large variety of new heavy resonances described in [51, 5] we choose the Z'_{SSM} within the Sequential Standard Model (SSM) [6], which has the same couplings as the Standard Model Z^0 and is often used as a benchmark by experimentalists. It is available in the PYTHIA generator [48]. The detector response is simulated with the GEANT4-based simulation sub-package of CMSSW [52], version 3_1_0. The digitization (simulation of the electronics response), the emulation of the Level- 1 and High-Level (HLT) Triggers, and the offline reconstruction are performed with the full

CMS reconstruction package CMSSW [52], version 3_1_0.

We make the usual assumption that the resonances decay only to three ordinary families of quarks and leptons and that no exotic decay channels are open. The cross sections for Z'_{SSM} is shown in Table 4.1 and are at leading order (LO), as predicted by PYTHIA. We scale them by a constant K factor of 1.35 in order to take into account the next-to-next-to-leading order (NNLO) QCD corrections. The full-interference $Z'/Z^0/\gamma^*$ samples used in this study are generated in broad mass intervals around the mass peak (above 400 GeV/c^2 for $M_{Z'} = 1$ TeV/c^2, above 600 GeV/c^2 for $M_{Z'} = 1.2$ TeV/c^2 and 1.3 TeV/c^2, and above 1 TeV/c^2 for $M_{Z'} = 2$ TeV/c^2).

Table 4.1: The product of the leading-order production cross section times branching ratio for Z'_{SSM} with masses $M_{Z'}$ of 1.0, 1.2, 1.3 and 2 TeV/c^2 for 7 TeV center-of-mass energy, as predicted by PYTHIA.

$M_{Z'_{SSM}}$ [TeV/c^2]	1.0	1.2	1.3	2.0
$\sigma^{LO}\times$ BR [fb] (PYTHIA)	137	40	29	2

The dominant (and irreducible) source of background to new high-mass dimuon resonances is Drell-Yan production of muon pairs, $pp \to \gamma^*/Z^0 \to \mu^+\mu^-$. Drell-Yan samples with two different cut-off values on the dimuon invariant mass are generated: $M_{\mu^+\mu^-} \geq 0.2$, 0.5 TeV/c^2. The total production cross section

times branching ratio in these two mass intervals are listed in Table 4.2.

Each of these samples including Z'_{SSM} signal samples include 50,000 events unless otherwise mentioned. These samples are reconstructed with ideal, startup, and 50 pb^{-1} alignments. All of these samples are hosted on the Open Science Grid by T3_US_FIT and are available in the Database Bookkeeping System (DBS) at DBS instances of cms_dbs_ph_analysis_02 [53] so that people affiliated with the CMS can access these datasets for their analysis.

Table 4.2: The product of the leading-order production cross section times branching ratio for Drell-Yan events with different cut-off values on the dimuon mass for 7 TeV center-of-mass energy, as predicted by PYTHIA.

$M_{\mu^+\mu^-}$ [TeV/c^2]	≥ 0.2	≥ 0.5
$\sigma^{LO}\times$ BR [fb] (PYTHIA)	1052	26

4.3 Event Selection

In order to efficiently select a pure sample of high-mass dimuon candidates, we require that:

- The event must pass the logical OR of single-muon and dimuon non-isolated trigger paths.
- It contain at least one pair of oppositely-charged muons reconstructed offline.
- The transverse momentum p_{T} of each muon track in a pair be larger than 20 GeV/c.
- Both muons be isolated in the tracker in such a way that the sum of the p_{T} of all tracks around each muon in a cone of $\Delta R = \sqrt{(\Delta\phi)^2 + (\Delta\eta)^2} < 0.3$ is required to be less than 10 GeV/c.

4.4 Results for Muon p_T and Dimuon Mass Resolutions with Misalignments

The precision of reconstructed dimuon mass, and consequently the statistical significance of a possible resonance peak, is affected by imperfect alignment of the tracker and the muon spectrometer. Small curvatures of high-momentum

tracks would be poorly constrained if the alignment of sensor and chamber positions is uncertain; a situation we expect to improve with a good amount of data.

To describe the expected misalignments and their improvement with time and integrated luminosity, several misalignment scenarios were developed in the CMS reconstruction framework in previous studies [54, 44, 55]. These misalignment scenarios are updated here to simulate the detector alignment expected to be achieved at startup and with 50 pb^{-1} of integrated luminosity. These updated scenarios take into account alignment expertise accumulated since the Physics TDR and, in particular with the results obtained during the Magnet Test and Cosmic Challenge (MTCC), and the Cosmic Run At Four Tesla (CRAFT) in 2008 and 2009. The results and the hardware constants derived from the muon alignment system in CRAFT 2008 are described in [28]. The uncertainties in the positions of muon chambers resulting from these alignment scenarios are then used in the reconstruction of high-p_T muons from Z' decays, with the corresponding tracker misalignment, to measure the transverse momentum resolution and the dimuon mass resolution.

The relative transverse momentum (p_T) resolution is obtained by a Gaussian fit to the distribution of the quantity

$$\left(\frac{q/p_T^{rec} - q/p_T^{gen}}{q/p_T^{gen}}\right), \tag{4.1}$$

where q is the muon charge, and p_T^{gen} and p_T^{rec} are the generated and reconstructed transverse momenta, respectively.

The dimuon mass resolution is obtained by a Gaussian fit to the distribution of the quantity

$$\left(\frac{M^{rec}_{\mu^+\mu^-} - M^{gen}_{\mu^+\mu^-}}{M^{gen}_{\mu^+\mu^-}}\right), \tag{4.2}$$

where $M^{gen}_{\mu^+\mu^-}$ and $M^{rec}_{\mu^+\mu^-}$ are the generated and reconstructed dimuon masses, respectively.

Before calculating the invariant mass of an opposite-sign muon pair, $M_{\mu^+\mu^-}$, a search for photon candidates in a cone with a radius of $\Delta R < 0.1$ around the trajectory of each muon is performed, and the 4-momentum of the photon candidate with the smallest ΔR in the cone is added to the 4-momentum of the muon. This procedure improves the invariant mass resolution by recovering some of the energy lost by the muon via final state radiation and radiative processes in the detector.

4.4.1 Z' Signal

The dimuon mass resolution and transverse momentum resolution for muons from Z' decay with several misalignment scenarios are presented in this section. One of the events from the simulated Z' with mass 1.2 TeV/c^2 decaying to two high p_T muons is shown in Figure 4.1.

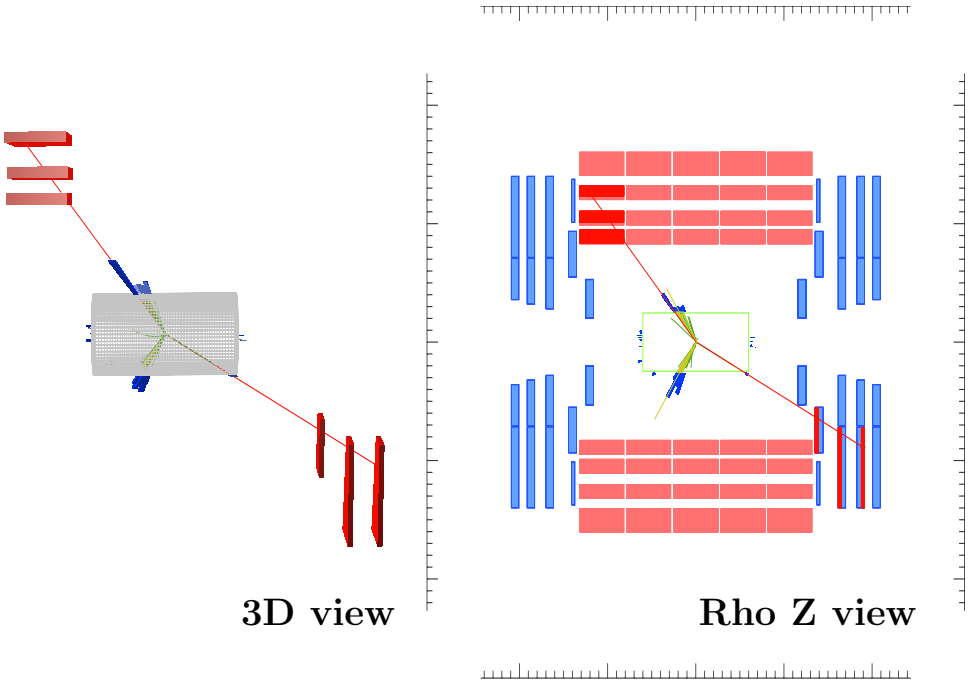

Figure 4.1: A simulated Z' event with $M^{gen}_{\mu^+\mu^-} = 1105$ GeV/c^2 in CMS, showing two high p_T (361.5 GeV/c and 354.5 GeV/c) muons (red lines) in two views. The event is reconstructed with startup alignment and the globally reconstructed dimuon mass is $M^{rec}_{\mu^+\mu^-} = 1078$ GeV/c^2.

The invariant mass resolution depends on the alignments of the silicon tracker and of the muon system. The dimuon mass resolution for 1.2 TeV/c^2 Z'_{SSM} resonance is shown in Figure 4.2 illustrating how the expected misalignment smears the distribution of the mass resolution. Current estimates of the alignment expected to be achieved with 50 pb^{-1} of integrated luminosity predict a mass resolution of 6-7% at $M_{\mu^+\mu^-} = 1$ TeV/c^2. We calculate the dimuon mass resolutions for a number of cases, with three alignment scenarios for three Z' signal mass points at 10 TeV and 7 TeV center-of-mass energy. These are tabulated in Table 4.3 as obtained from three muon reconstruction algorithms; Global reconstruction (GR), Tracker only (TK) and tracker-plus-first-muon station (FS) [37].

We have also studied the transverse momentum resolutions for muons from the Z' decay for various combinations of alignments, center-of-mass energies, and Z' masses. The p_T resolutions are studied separately in the endcap and barrel regions. We are mostly focusing on the endcap. The p_T resolutions for the endcap muons are shown in Figure 4.3, where the effect of misalignments is clearly seen.

Table 4.3 summarizes our results for muon p_T resolutions in the endcap at 7 TeV and 10 TeV center-of-mass energies with three alignment scenarios (ideal, startup, and the $50\,pb^{-1}$) for three Z' signal samples ($M_{Z'} = 1.0$, 1.2, 1.3 TeV/c^2). The last three columns show the momentum resolutions as ob-

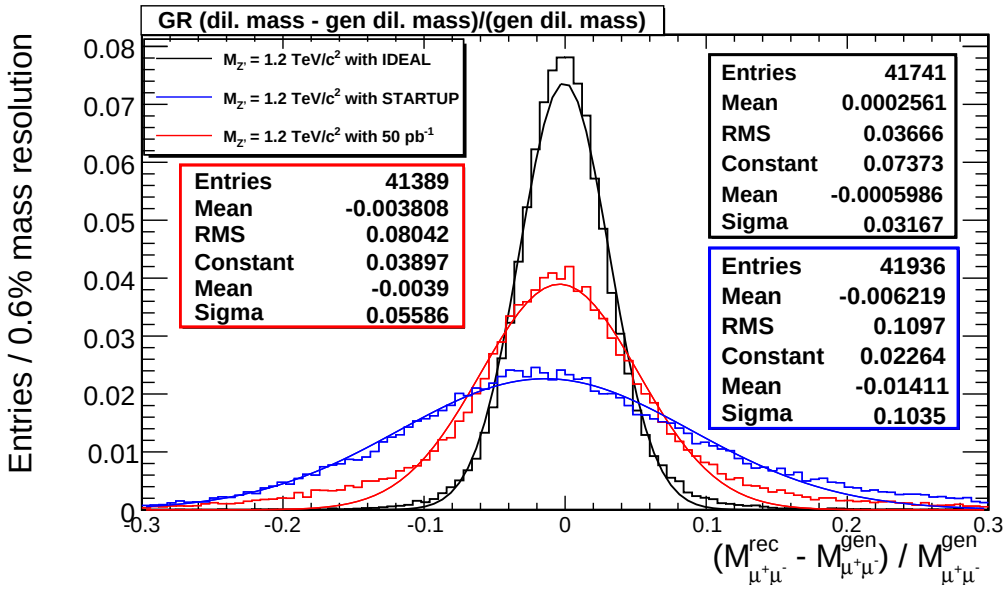

Figure 4.2: Normalized invariant mass resolution for 1.2 TeV/c^2 Z'_{SSM}. The events shown here are reconstructed with three alignment scenarios: ideal (black), startup (blue) and 50 pb^{-1} (red) indicating the considerable effect of muon misalignment.

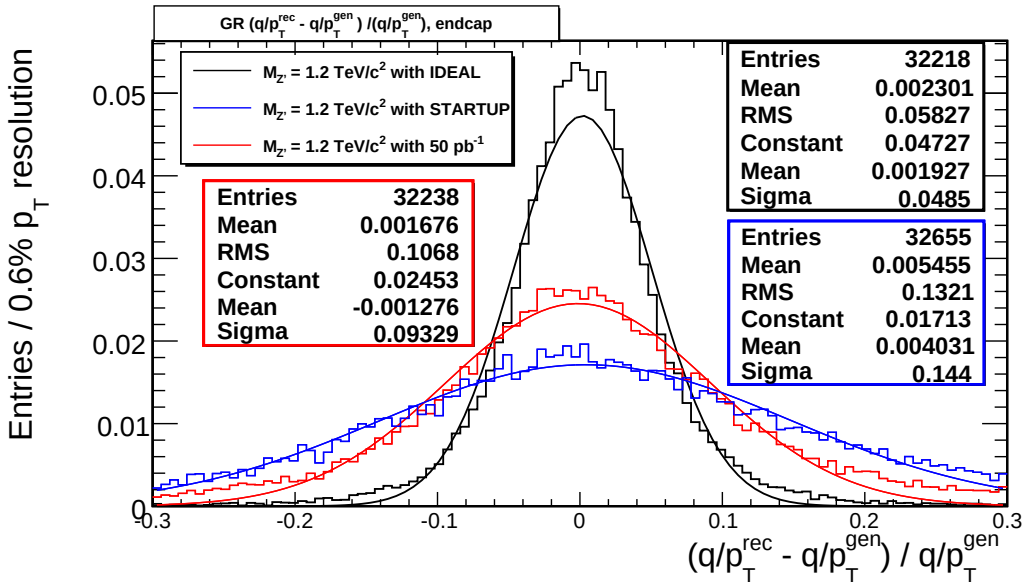

Figure 4.3: Normalized relative p_T resolution for endcap muons from 1.2 TeV/c^2 Z'_{SSM} simulated with three different alignment scenarios: ideal (black), startup (blue) and 50 pb^{-1} (red).

Table 4.3: Summary of Z' mass and muon endcap p_T resolution studies for different alignment scenarios, muon reconstruction algorithms (global reconstruction "GR", Tracker only "TK", and tracker plus the first muon station "FS") and center-of-mass energies.

Z′ Mass	Alignment	CM energy	Dimuon Mass Resolution (%)			Muon Endcap p_T Resolution (%)		
(TeV/c²)	Scenario	(TeV)	GR	TK	FS	GR	TK	FS
	IDEAL	10	3.0	3.5	2.9	4.6	5.1	4.5
		7	2.6	3.1	2.5	3.9	4.4	3.8
1.0	50 pb^{-1}	10	6.6	11.1	6.0	10.6	16	9.9
		7	6.2	9.4	5.2	9.8	13.6	8.9
	STARTUP	10	10.2	11.1	8.5	13.9	16	10.9
		7	8.9	9.4	7.4	12.9	13.4	9.7
	IDEAL	10	3.0	3.5	2.9	4.6	5.1	4.5
		7	3.2	3.9	3.1	4.8	5.1	4.7
1.2	50 pb^{-1}	10	6.7	11.1	6.0	10.6	16	9.9
		7	5.6	11.2	6.1	9.3	14.9	9.4
	STARTUP	10	10.2	11.1	8.5	13.9	16	10.9
		7	10.3	11.4	8.1	14.4	15.9	9.9
	IDEAL	10	3.4	4.4	3.3	5.3	6.3	5.2
		7	3.2	4.1	3.1	4.4	4.9	4.4
1.3	50 pb^{-1}	10	6.7	13.3	6.3	10.7	18.9	10.6
		7	6.0	11.3	5.7	8.4	16.1	9.4
	STARTUP	10	11.8	13.3	10.3	15.2	18.9	12.0
		7	10.5	11.3	9.6	14.2	16.2	10.4

tained from three muon reconstruction algorithms; Global reconstruction (GR), Tracker only (TK) and tracker-plus-the-first-muon station (FS). From Table 4.3 we conclude that

- Resolutions improve significantly from the startup alignment to the $50\,pb^{-1}$ alignment by 3.5 %
- For a given alignment, the resolutions are independent of the center-of-mass energy
- Inclusion of the first muon station in the track fit improves the resolution dramatically, which illustrates the importance of muon tracking for high p_T muons

4.4.2 High-Mass Drell-Yan Background

The globally reconstructed (GR) invariant mass spectra for Drell-Yan events with $M^{gen}_{\mu^+\mu^-} > 500\,GeV/c^2$ are shown in Figure 4.4. The global muon reconstruction uses information for the muon system and also silicon tracker hits. The reconstruction is performed with three different alignment scenarios: ideal, startup, and $50\,pb^{-1}$.

The p_T resolutions are studied separately in the endcap and barrel regions. We mostly focus on the endcap here. The global muon p_T resolutions in the Barrel and Endcap for Drell-Yan events with $M^{gen}_{\mu^+\mu^-} > 500$ GeV/c^2 with three

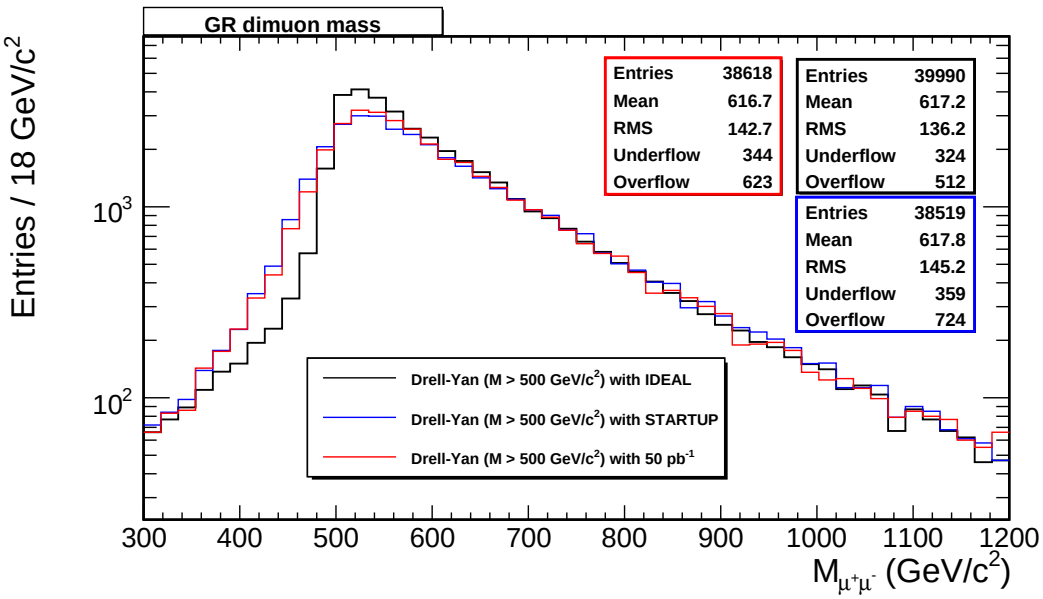

Figure 4.4: The globally reconstructed (GR) invariant mass spectra for the Drell-Yan events with invariant mass $M^{gen}_{\mu^+\mu^-} > 500$ GeV/c^2. The alignment scenarios are ideal (black), startup (blue), and $50\,pb^{-1}$ (red). These plots are normalized to the same number of events.

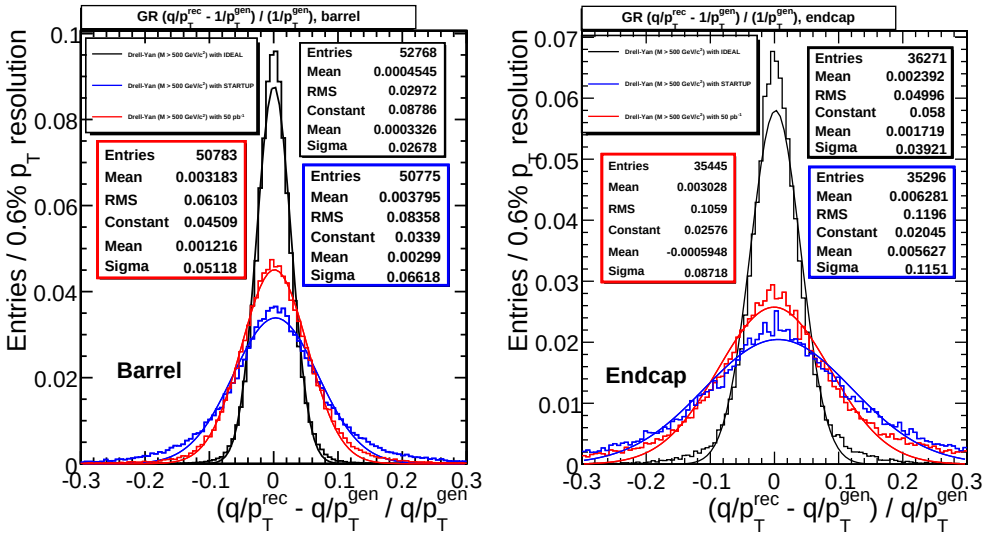

Figure 4.5: Normalized p_T resolution spectra for muons in Barrel only (left) and Endcap only (right) for Drell-Yan events with $M^{gen}_{\mu^+\mu^-} > 500$ GeV/c^2 at $\sqrt{s} = 7$ TeV. The events shown here are for ideal (black), startup (blue), and $50\,pb^{-1}$ (red) alignment scenarios. The p_T resolutions for muons in the endcap are 3.9%, 11.5%, and 8.7% for ideal, startup, and $50\,pb^{-1}$ alignment scenarios, respectively.

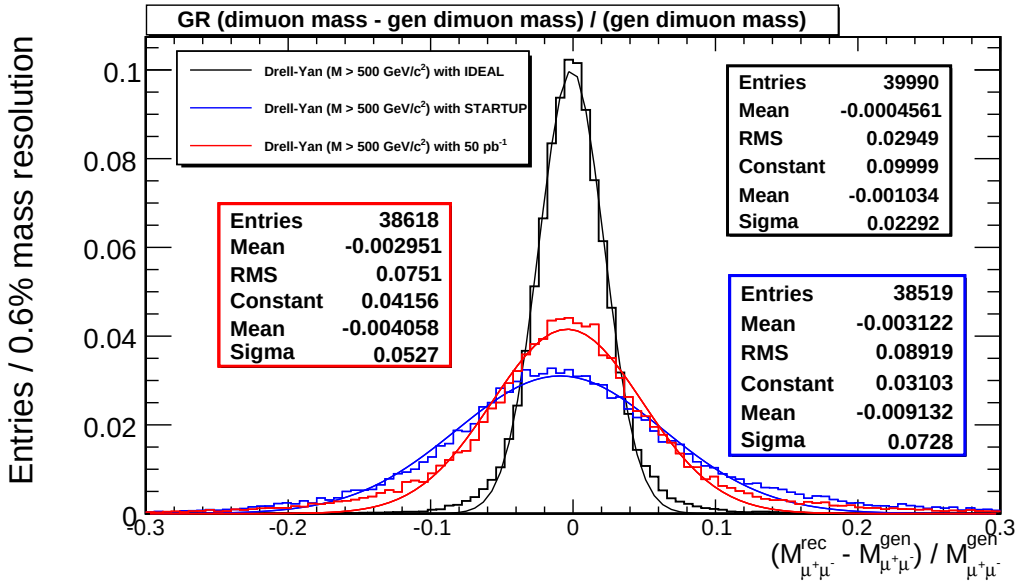

Figure 4.6: The invariant mass resolution spectra for Drell-Yan events with $M^{gen}_{\mu^+\mu^-} > 500$ GeV/c^2 at $\sqrt{s} = 7$ TeV. The events shown here are reconstructed with three alignment scenarios: ideal (black), startup (blue) and $50\,pb^{-1}$ (red) indicating the considerable effect of muon misalignment in the different scenarios.

different alignments are shown in Figure 4.5. The p_T resolutions in the Barrel and Endcap for the startup scenario are 6.6% and 11.5%, respectively. In the endcap, the resolutions for each alignment are worse than those in the barrel, as expected.

The mass resolution spectra for Drell-Yan with $M^{gen}_{\mu^+\mu^-} > 500$ GeV/c^2 are shown in Figure 4.6. The spectra show the considerable impact of muon and tracker misalignments for the three different alignment scenarios. The invariant mass resolutions for Drell-Yan events with $M^{gen}_{\mu^+\mu^-} > 500$ GeV/c^2 for ideal, startup, and $50\,pb^{-1}$ are found to be 2.3%, 7.3%, and 5.3%, respectively.

4.5 Muon Endcap Alignment Systematics and p_T Resolution

We have studied the impact of anticipated muon endcap alignment systematics, i.e. how systematic biases in the muon endcap positions will affect the muon p_T resolutions. For this study, only the muon endcap is misaligned with respect to the existing ideal or startup muon geometry. Individual muon endcap yoke disks (stations) and also entire endcaps are misaligned in position (x_{CMS}, y_{CMS}, z_{CMS}) up to $\pm\,2$ mm or rotated in $\phi_{z_{CMS}}$ i.e. around the beam line, up to $\pm\,0.5$ mrad with steps of 0.1 mm and 0.1 mrad, respectively. The selection of these numbers is motivated by the current startup muon endcap alignment

uncertainties, which are 0.5 -1.0 mm in position (Δx_{CMS}, Δy_{CMS}, Δz_{CMS}) and 0.1 mrad in $\Delta\phi_{z_{CMS}}$. These numbers are also motivated by the CRAFT 2008 study [28]. A recently discovered bug in the track-based alignment procedure related to the inclusion of RPC hits in the track fitting indicated a systematic alignment shifts up to 1.5 mm [56], i.e. of similar magnitude.

The method for this study is as follows:

1. A standard CMSSW-readable muon geometry in an SQLite file is converted into a human-readable XML file using a tool described in [57]. The XML file is modified according to our intended misalignments and converted back to an SQLite file. Thus, a modified muon geometry with each intended misalignment is generated and saved in the form of an SQLite database file.

2. A Z' signal sample ($M_{Z'_{SSM}}$ = 1.2 TeV/c^2 or 2.0 TeV/c^2) is fully reconstructed with a customized global tag with modified SQLite file corresponding to the ideal or startup alignment.

3. The analysis code is re-run over the resulting biased MC data set for each case repeatedly. We obtain the results for different reconstructions: Global reconstruction (GR), Tracker-only (TK) and Tracker plus the First Muon Station (FS). Tracker-only (TK) is driven by measurements in the silicon tracker only. Global muon reconstruction (GR) is based on a combined

fit to selected hits in the muon system and the silicon tracker. Another approach of refitting the global-muon track ignoring hits in all muon stations except the innermost one containing hits is called the "tracker plus the first muon station" (FS) fit.

First, we verify our procedure by comparing the results with bias in the endcap and without the bias. In order to do so, we have to get identical results in the barrel and tracker-only reconstruction results, where we do not impose any bias. The width of relative muon p_T resolutions as a function of pseudorapidity (η) are plotted in Figure 4.7. The top plot is without bias (ideal alignment) and the bottom plot is with 2 mm systematic bias to all Muon Endcap stations in x_{CMS}. The central regions are identical in both plots but in the endcap ($|\eta| > 1$) the resolutions have become worse due to the bias except in the tracker-only reconstruction, as expected. These facts confirm that the reconstruction is performing as intended.

Next, we discuss p_T resolutions as a function of p_T. Again, we compare the results with the bias and without it. Figure 4.8 shows the comparison of the Gaussian widths of q/p_T relative resolution for muons in each p_T bin with and without bias for ideal alignment. It is clearly seen that the bias of 2 mm deteriorates the muon p_T resolutions. This effect becomes prominent for $p_T > 200$ GeV/c. Since we are concerned with different alignment scenarios, the most relevant scenario to study the effect of misalignment is the startup

alignment. The corresponding plot for the muon p_T resolution vs. p_T using the decay of a 2 TeV/c^2 Z' but reconstructed with startup alignment is shown in Figure 4.9. We obtain a resolution of 10-20% for $p_T > 200$ GeV/c with startup alignment, whereas 4-6% is found with ideal alignment for the same p_T range.

Table 4.4: Gaussian width (σ) of relative p_T resolution in (%) in the Endcap for biases on all eight Muon Endcap station positions for ideal and startup alignment geometries.

Bias Δx_{CMS} [mm]	0	2.0	−2.0	1.5	−1.5	1.0	−1.0	0.5	−0.5
Ideal	4.8	6.5	6.6	6.2	6.2	5.7	5.7	5.1	5.1
Startup	14.9	18.4	15.8	17.9	14.9	17	14.4	16	14.3

Table 4.5: Gaussian width (σ) of relative p_T resolution (%) in Endcap for biases on all eight Muon Endcap station orientations for ideal and startup alignment geometries.

Bias $\Delta\phi_{z_{\mathrm{CMS}}}$ [mrad]	0	0.5	−0.5	0.4	−0.4	0.3	−0.3	0.2	−0.2	0.1	−0.1
Ideal	4.8	7.4	7.4	7	7	6.3	6.4	5.9	5.6	5.1	5.1
Startup	14.9	20.5	17.6	18.9	16.4	17.4	15.5	16.2	15	15.4	14.8

We quantify the effect of bias in the muon endcap alignment on the p_T resolution for muons in the endcap. We bias the position of one endcap station

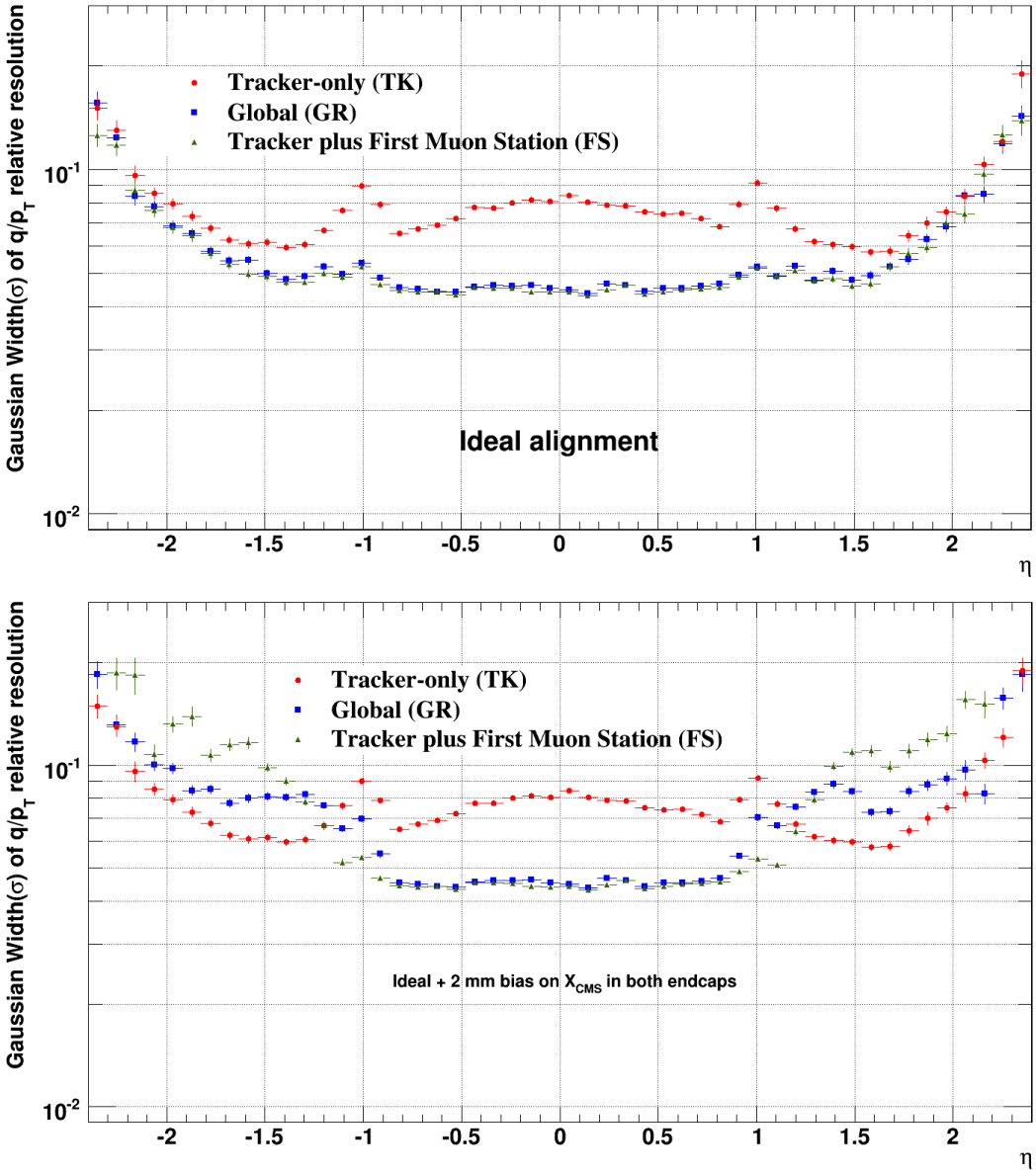

Figure 4.7: Relative muon p_T resolution vs. η for barrel and endcap muons based on Gaussian widths of $(q/p_T(\text{rec.}) - q/p_T(\text{gen.}))/(q/p_T)(\text{gen.})$ distributions for each p_T bin using the MC sample for $M_{Z'} = 2$ TeV/c^2 and three muon reconstructions for ideal alignment scenario (top) and with 2 mm systematic bias in x_{CMS} to all Muon Endcap stations (bottom)

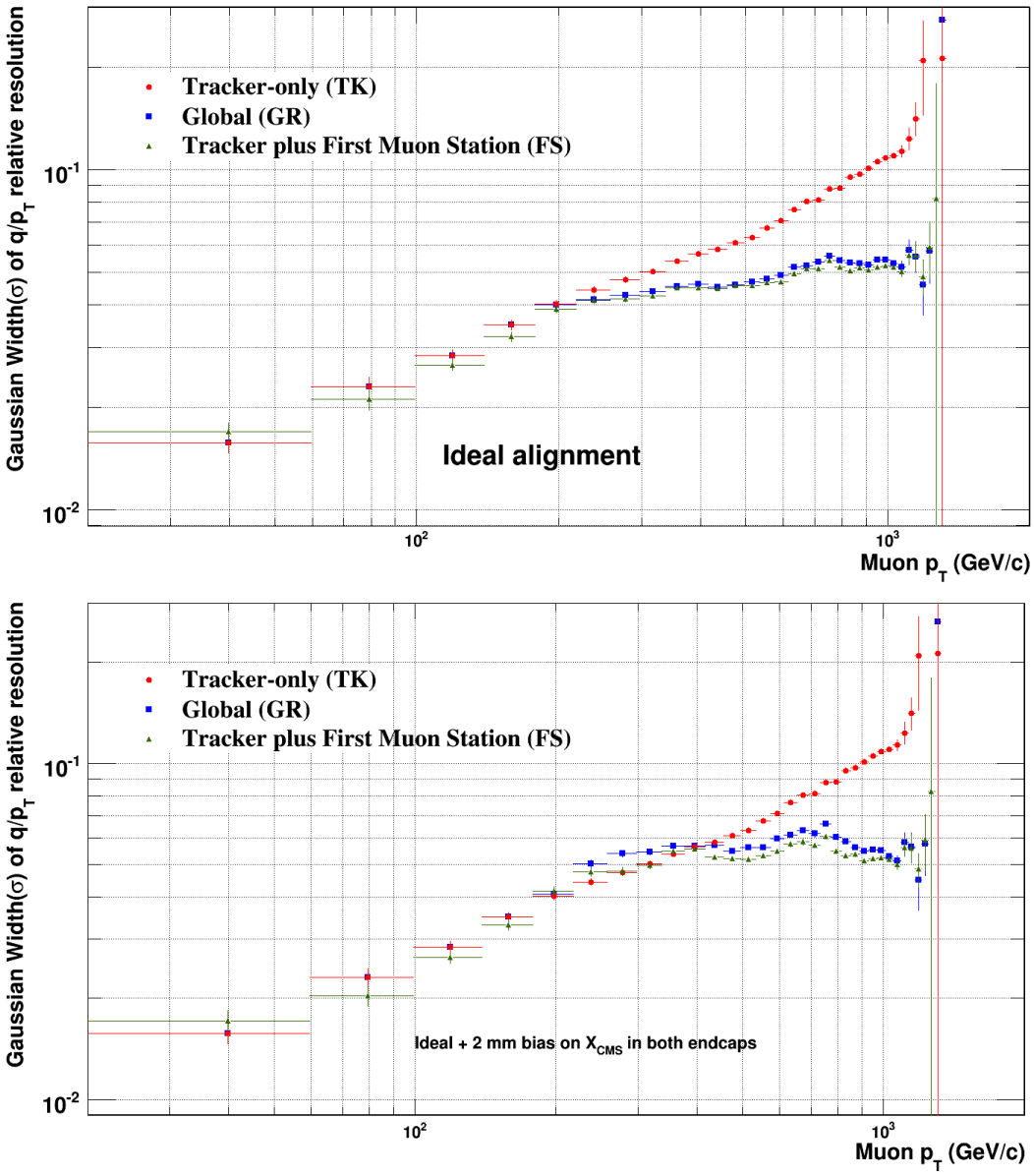

Figure 4.8: Relative muon p_T resolution vs. p_T for barrel and endcap muons based on Gaussian widths of $(q/p_T(\text{rec.}) - q/p_T(\text{gen.}))/(q/p_T)(\text{gen.})$ distributions for each p_T bin using the MC sample for $M_{Z'} = 2$ TeV/c^2 and three muon reconstructions for ideal alignment scenario (top) and with 2 mm systematic bias in x_{CMS} to all Muon Endcap stations (bottom)

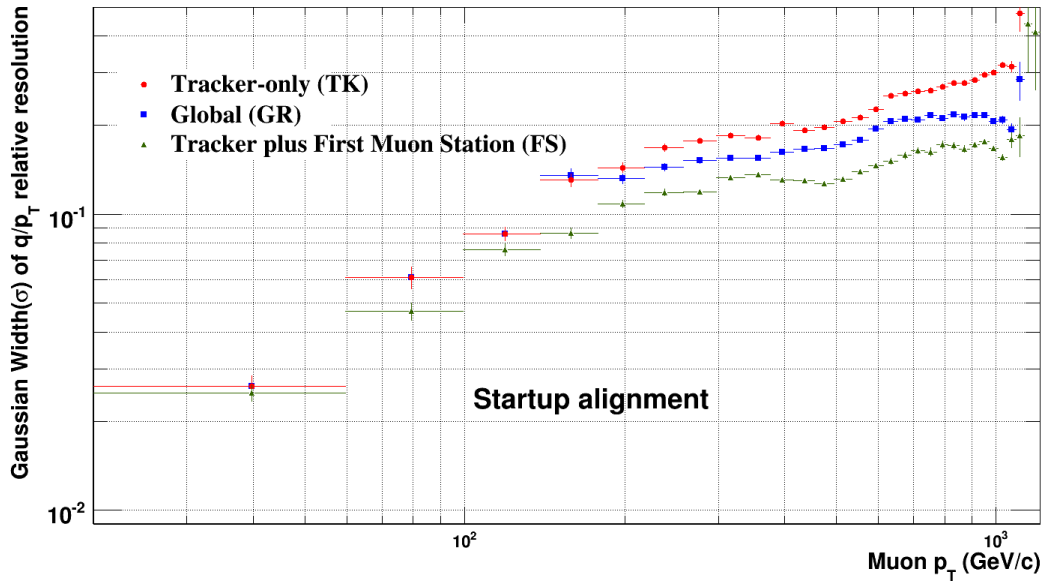

Figure 4.9: Relative muon p_T resolution vs. p_T for barrel and endcap muons based on Gaussian widths of $(q/p_T(\text{rec.}) - q/p_T(\text{gen.}))/(q/p_T)(\text{gen.})$ distributions for each p_T bin using the MC sample for $M_{Z'} = 2$ TeV/c^2, startup alignment scenario, and three muon reconstructions.

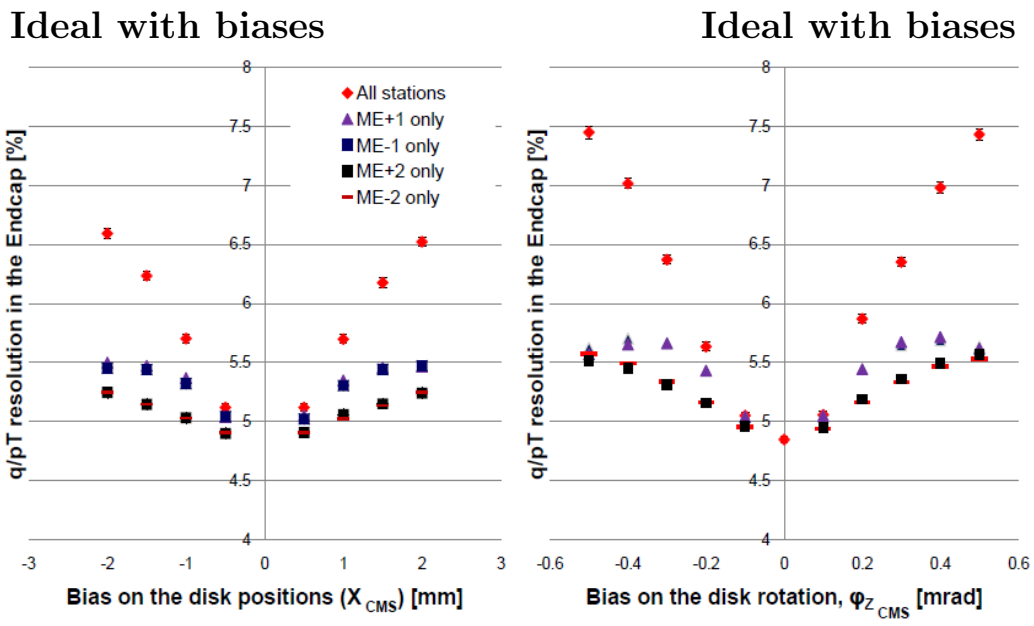

Figure 4.10: Relative muon p_T resolution vs. biases in the ideal endcap disk alignment for endcap muons based on Gaussian widths of $(q/p_T(\text{rec.}) - q/p_T(\text{gen.}))/q/p_T(\text{gen.})$ distributions using the MC sample for $M_{Z'} = 2$ TeV/c^2. Plots are for bias on muon endcap disk positions x_{CMS} (left) and bias on the disk rotation $\phi_{z_{CMS}}$ (right) applied to all Muon Endcap stations or individual stations ME+1, ME-1, ME+2, and ME-2.

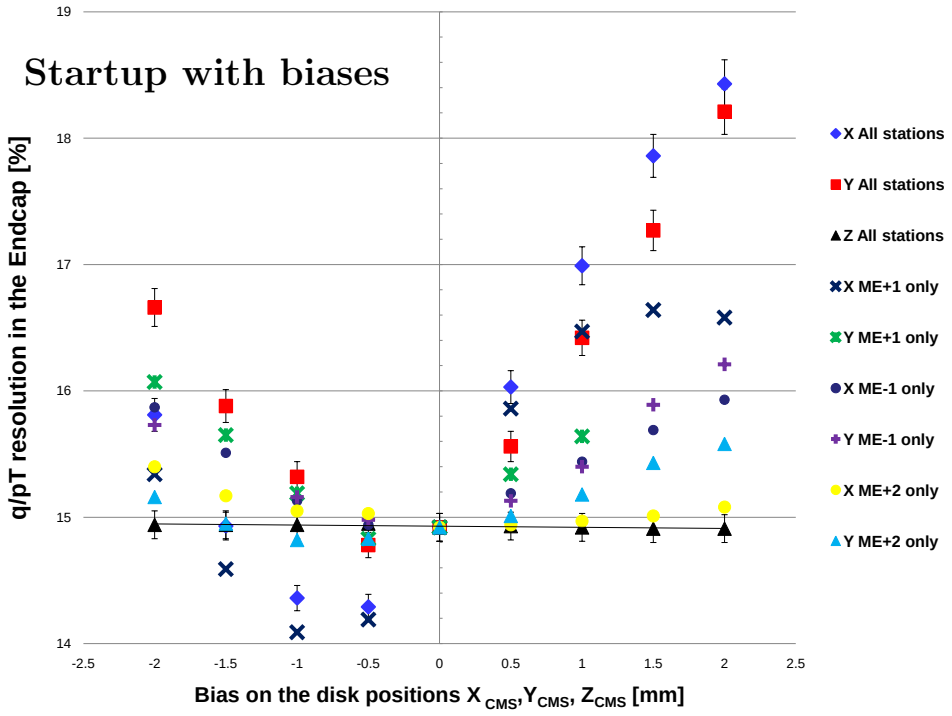

Figure 4.11: Relative muon p_T resolution vs. biases in startup endcap disk alignment for endcap muons based on Gaussian widths of $(q/p_T(\text{rec.})\text{-}q/p_T(\text{gen.}))/q/p_T(\text{gen.})$ distributions using the MC sample for $M_{Z'} = 2$ TeV/c^2. This plot shows the effect of biases on muon endcap disk positions x_{CMS}, y_{CMS}, and z_{CMS} applied to all Muon Endcap stations or individual stations ME+1, ME-1, ME+2, and ME-2.

(eg. ME+1 only) or all endcap stations in x_{CMS} with respect to ideal (or startup). Using the 2 TeV/c^2 Z' sample we analyze the Gaussian width of relative resolution for endcap muons repeatedly with biases of different sizes (0.5 - 2 mm). Also, we bias the position of entire endcap stations and repeat the analysis procedure. Figure 4.10 shows the p_T resolution for muons in the endcap as a function of bias in x_{CMS} and $\phi_{z_{CMS}}$. This figure illustrates the effect of biases on the position of entire endcap stations and individual station ME+1, ME-1, ME+2, and ME-2. The largest effect is seen when all muon endcaps are biased together, as expected. With a similar bias to either ME+1 or ME-1, the effect is identical, which is also true for ME2. The effect becomes less significant as the biased station is farther from the interaction point. Table 4.4 summarizes the p_T resolution in % for each bias in the position x_{CMS} of the entire endcap with respect to ideal and startup alignment scenarios. As the bias increases, it deteriorates the muon p_T resolution by 2% for 2 mm systematic bias in x_{CMS} relative to all muon endcap stations for an ideal alignment. We find similar results with the bias in the position y_{CMS} as with the bias in position x_{CMS} for an ideal alignment. We find insignificant change on the p_T resolution for muons when we bias the position of the entire endcaps in z_{CMS}. Similarly, Table 4.5 summarizes the p_T resolution in % for each bias in the rotation $\phi_{z_{CMS}}$ of the entire endcap with respect to ideal and startup alignment scenarios.

With respect to ideal alignment, we find symmetrical results. But we obtain

asymmetric results with respect to the startup alignment for the same positive and negative bias as shown in Figure 4.11, which summarizes our systematic study of biases on muon endcap disk positions x_{CMS}, y_{CMS}, and z_{CMS} to all endcap stations or individual station ME+1, ME-1, ME+2, and ME-2 with respect to startup alignment. When we bias the position of all stations by 2 mm, the muon p_T resolution in the endcap worsens by 3%. In the case of startup alignment, we bias the position of disks in x_{CMS} and y_{CMS} and quantify their effect on the muon p_T resolution. We find asymmetrical results for positive bias and negative bias and also for the same bias in x_{CMS} and y_{CMS}.

4.6 CMS Discovery Potential in $Z' \rightarrow \mu^+\mu^-$ Channel

4.6.1 Dimuon Mass Spectra and Fitting Procedure

An example of the dimuon mass $M_{\mu^+\mu^-}$ spectra for the full interference $Z'/Z^0/\gamma^*$ signal sample ($M_{Z'} = 1.2$ TeV/c^2) and Drell-Yan background only samples are shown in Figure 4.12. Both are reconstructed with the startup alignment. For the significance analysis, we use a background sample that is the weighted sum of these two background data sets.

Another example of dimuon mass spectra for the full interference $Z'/Z^0/\gamma^*$

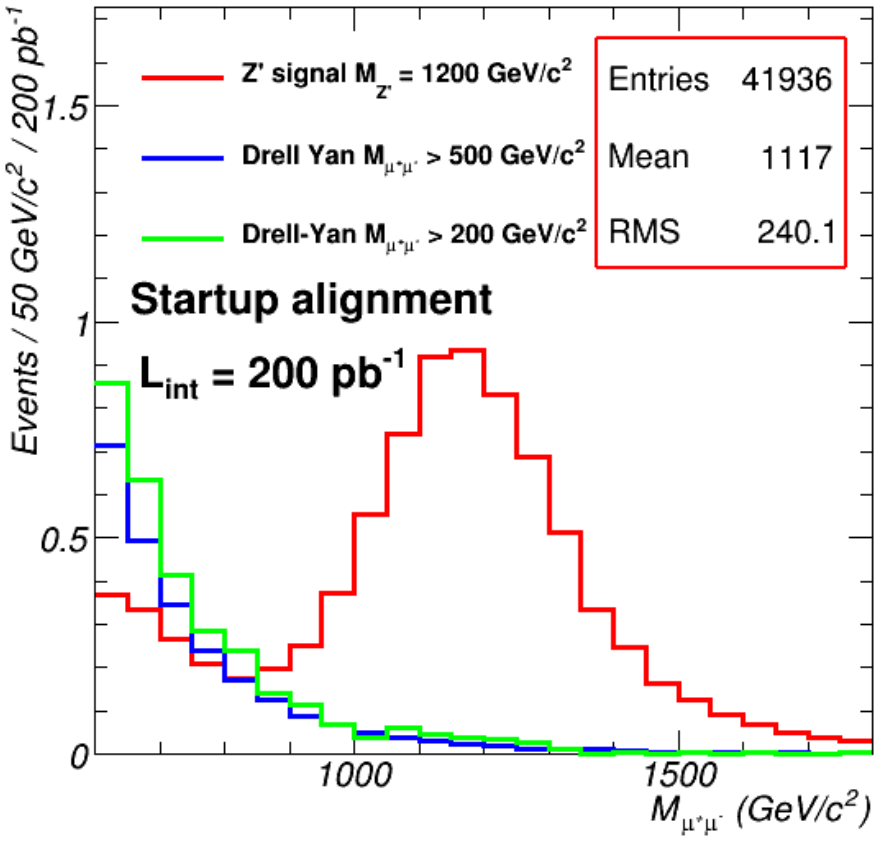

Figure 4.12: Histograms of the globally reconstructed dimuon invariant mass for the full interference $Z'/Z^0/\gamma^*$ signal sample ($M_{Z'}$=1.2 TeV/c^2) and Drell-Yan background Monte Carlo samples ($M_{\mu^+\mu^-} > 200$ GeV/c^2 and 500 GeV/c^2). The number of events per bin is normalized to an integrated luminosity of 200 pb^{-1}.

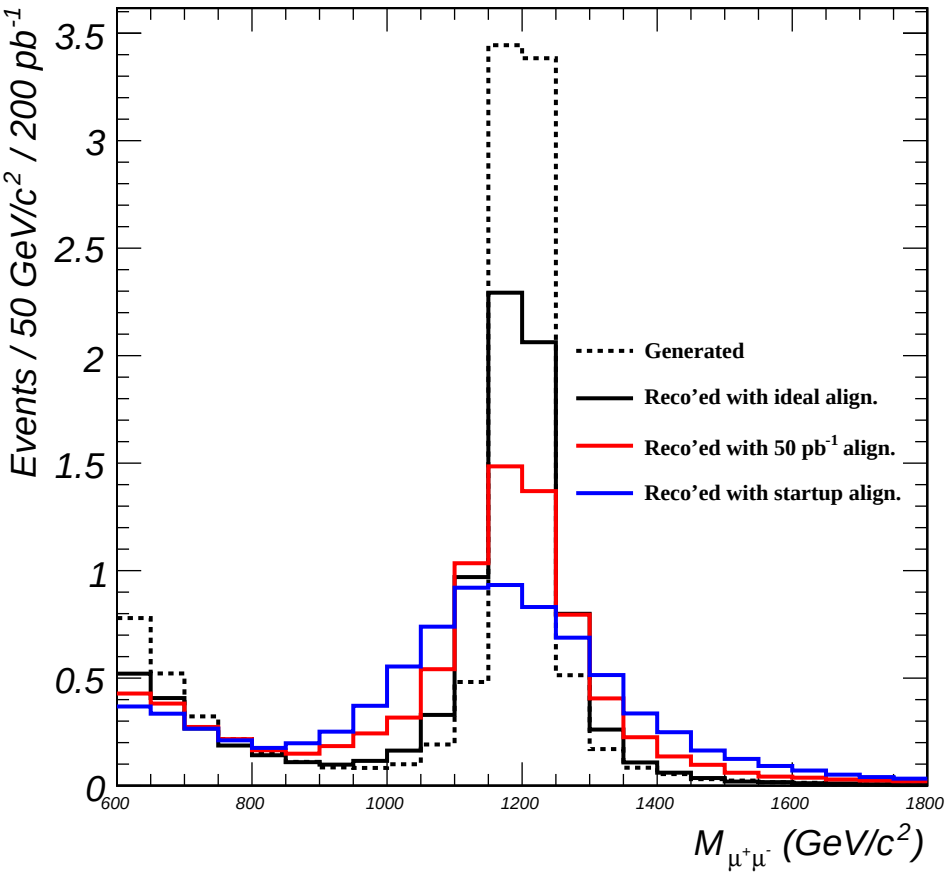

Figure 4.13: Histograms of the dimuon invariant mass for the full interference $Z'/Z^0/\gamma^*$ signal sample ($M_{Z'}$=1.2 TeV/c^2) at the event-generator level (dotted black line) and fully reconstructed with different alignments (solid lines with different colors). The number of events per bin is normalized to an integrated luminosity of 200 pb^{-1}.

signal for mass $M_{Z'} = 1.2$ TeV/c^2, with or without detector and reconstruction related effects, is shown in Figure 4.13. The dotted black line in the plot shows the generated mass spectrum (100 % efficiency with no detector and reconstruction related effects). It is compared with fully reconstructed events for different alignment scenarios, i.e. ideal, 50 pb^{-1}, and startup alignments. Figure 4.13 clearly shows the effect of alignment on the mass resolution and how the peaks get widened with worsening alignment.

We focus on the regime close to the discovery limit, which is characterized by a modest number of accumulated events. We use ensembles of Monte Carlo pseudo-experiments selected from the large-statistics signal and background samples. The number of events in each experiment, N_{evt}, fluctuates according to a Poisson distribution with a mean of $\sigma \times$ Br $\times \int Ldt \times \epsilon$, where $\int Ldt$ is the integrated luminosity and ϵ is the combined trigger and reconstruction efficiency. The mass distribution is composed of $M_{\mu^+\mu^-}$ values for N_{evt} events satisfying all selection criteria and not yet used in previous MC pseudo-experiments.

An unbinned maximum likelihood fit of the $M_{\mu^+\mu^-}$ values in each MC experiment is appropriate to test for the existence of a resonance and to measure its parameters if it is found to exist. We follow the methods discussed in section 5 of [55] for the fitting of dimuon mass spectra. As a model of the probability density function (pdf), p, of the parent population of the observed mass spectra,

we use

$$p\left(M_{\mu^+\mu^-};\, f_s, m_0, \Gamma, \sigma\right) = f_s \cdot\, p_s(M_{\mu^+\mu^-}; m_0, \Gamma, \sigma) + (1 - f_s) \cdot\, p_b(M_{\mu^+\mu^-}) \quad (4.3)$$

where p_s is the pdf of the signal, is a convolution of a Breit-Wigner signal resonance shape with a Gaussian accounting for mass resolution smearing; and p_b is the pdf of the background, is modeled as an exponential, $e^{-k\cdot M_{\mu^+\mu^-}}$, with the parameter k determined from fits to Drell-Yan events. This pdf, using k=2.0, gives a good description of the background shape in the whole mass region between 400 and 5000 GeV/c^2 [45].

There are three free parameters in the fit: the signal fraction $f_s = N_s/(N_s + N_b)$, the mass peak m_0, and the full-width-at-half-maximum (FWHM), Γ, of the signal. The shape of the background distribution is fixed, while its level is determined by the fit: f_s is a free parameter. Therefore, the fit explores the difference in shape between the signal and the background.

4.6.2 Z' Signal Significance Analysis

We use a signal significance estimator $S_{\mathcal{L}}$ based on log-likelihood ratio, which was found to perform well in the search for Z' bosons from the previous study described in [58]:

$$S_{\mathcal{L}} = \sqrt{2\ ln\ (\mathcal{L}_{s+b}/\mathcal{L}_b)}\,, \quad (4.4)$$

where $\mathcal{L}_{s+b}$ is the maximum likelihood value obtained in the full signal-plus-background unbinned maximuom likelihood fit, and $\mathcal{L}_b$ is the maximum likelihood from the unbinned background only fit.

We use the method described in section 4.6.1 and the likelihood ratio estimator $S_{\mathcal{L}}$ to evaluate the CMS discovery potential for $Z' \to \mu^+\mu^-$. We calculate the statistical significance of various expected signal and background samples by using Monte Carlo calculation and fits described in section 4.6.1. The procedure resulted in a computed mass range in which CMS can discover Z' bosons with a given amount of data for different detector alignment scenarios or correspondingly the required integrated luminosity to discover a Z' of a certain mass for different detector alignment scenarios.

Table 4.6: Average values of the log-likelihood ratio significance estimator $S_{\mathcal{L}}$ for the Z'_{SSM} at two signal mass points for an integrated luminosity of 200 pb^{-1} with three alignment scenarios.

	$\boldsymbol{Z'_{SSM}}$ **mass**	
Alignment Scenario	1.0 TeV/c^2	1.2 TeV/c^2
Startup	6.7	4.0
50 $\boldsymbol{pb^{-1}}$	7.8	4.5
Ideal	8.1	4.6

All available Z' samples with different masses and misalignment scenarios are

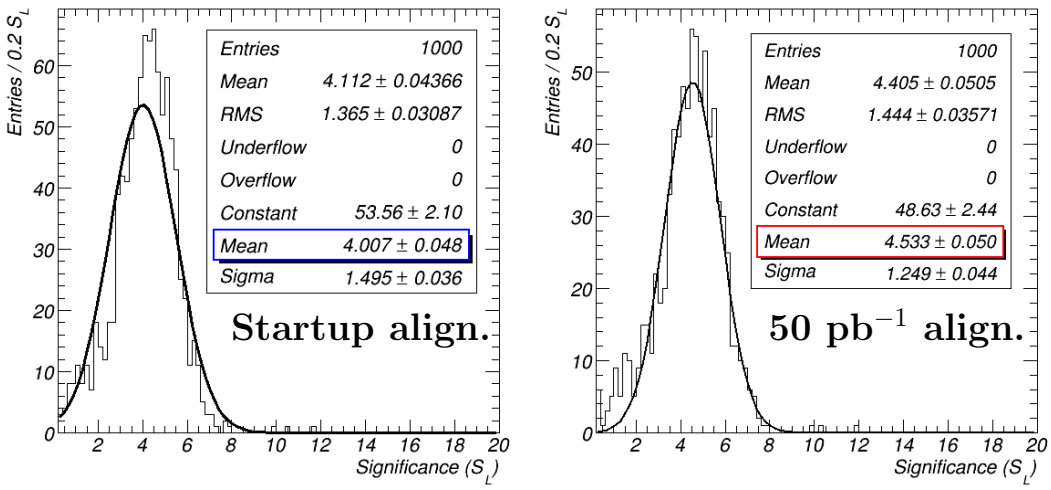

Figure 4.14: Histograms of signal significance for 1000 pseudo-experiments with the Gaussian fit for a 1.2 TeV/c^2 Z'_{SSM} for an integrated luminosity of 200 pb^{-1} with startup (left) and 50 pb^{-1} (right) alignments.

considered; the evaluation is repeated for several integrated luminosities. Two examples of signal significance distributions with the Gaussian fit, obtained from fits to a 1.2 TeV/c^2 Z'_{SSM} for an integrated luminosity of 200 pb^{-1} with startup alignment and with 50 pb^{-1} alignment, are shown in Figure 4.14. A summary of the signal significance expected for the Z'_{SSM} at two signal mass points for an integrated luminosity of 200 pb^{-1} with startup, 50 pb^{-1}, and ideal alignment scenarios are tabulated in Table 4.6. We note that better alignment improves the signal significance.

We use the same combinations of luminosities and misalignment scenarios to calculate the integrated luminosity needed to reach 5σ significance ($S_{\mathcal{L}} = 5$) for

a Z'_{SSM} discovery. In Figure 4.15, the signal significance is plotted as a function of integrated luminosity for two signal mass points for startup alignment and 50 pb^{-1} alignment. The data points are fitted by a spline curve and the integrated luminosity required for 5σ is extracted for a given alignment. For example, on the average 250 pb^{-1} data are required to discover a Z' with mass M = 1.2 TeV/c^2 assuming the 50 pb^{-1} alignment from the Figure 4.15 (right). The integrated luminosity needed to reach 5σ significance as a function of Z'_{SSM} mass for three different alignment scenarios is shown in Figure 4.16, which is our summary plot for the discovery potential and the effect of alignment on the Z' search.

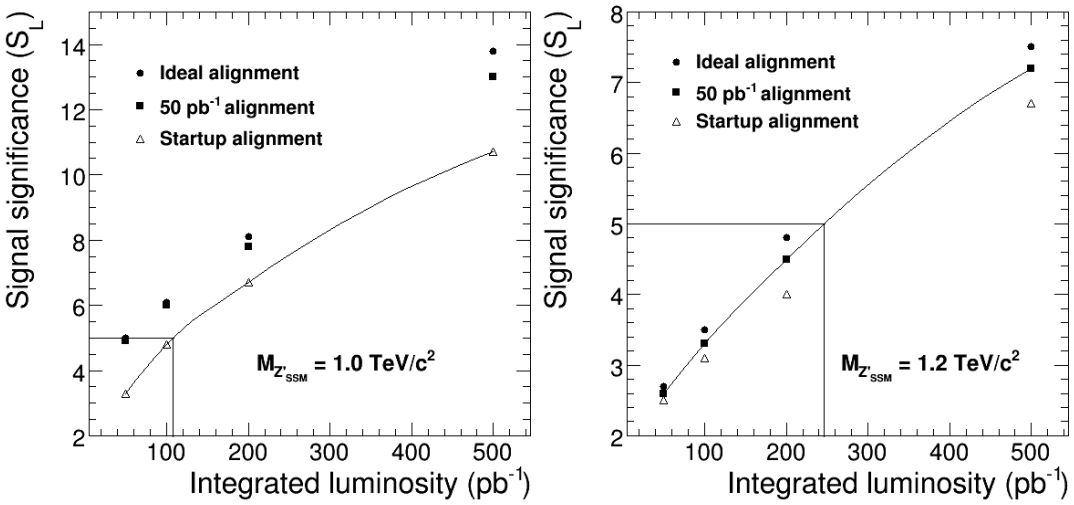

Figure 4.15: Signal significance as a function of the integrated luminosity and the alignment scenarios; the integrated luminosity needed to reach on the average 5σ significance ($S_{\mathcal{L}} = 5$) for the Z'_{SSM} is indicated.

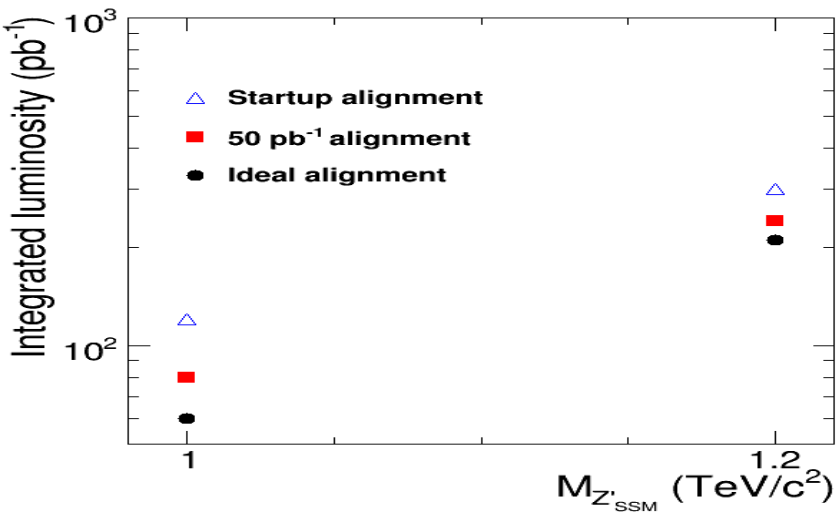

Figure 4.16: Integrated luminosity needed to reach 5σ significance ($S_{\mathcal{L}} = 5$) as a function of the mass of the Z'_{SSM} resonance reconstructed with ideal, startup, and 50 pb^{-1} alignments.

From Figure 4.16, we conclude that

- A better aligned detector requires less data to reach the same signal significance.
- 80 pb^{-1} of data, and the tracker and the muon detectors aligned with 50 pb^{-1} should be sufficient to discover a Z'_{SSM} at 1 TeV/c^2.
- At least 250 pb^{-1} data are required to observe Z'_{SSM} boson with mass M=1.2 TeV/c^2.

Muon Endcap Misalignments and the Z'_{SSM} Signal Significance

We have also used the samples with systematic muon endcap misalignment biases and calculated the average Z'_{SSM} (M=1.2 TeV/c^2) signal significance. The signal significance is plotted in figure 4.17 against the biases in position (left) and rotation around the beam line (right) of the entire endcap disks. It can be seen that the significance is sensitive to the misalignment of muon endcaps, but the effect is very small for our studied range of the misalignments, i.e. up to 2 mm in translation and up to 0.5 mrad in rotation around the beam line.

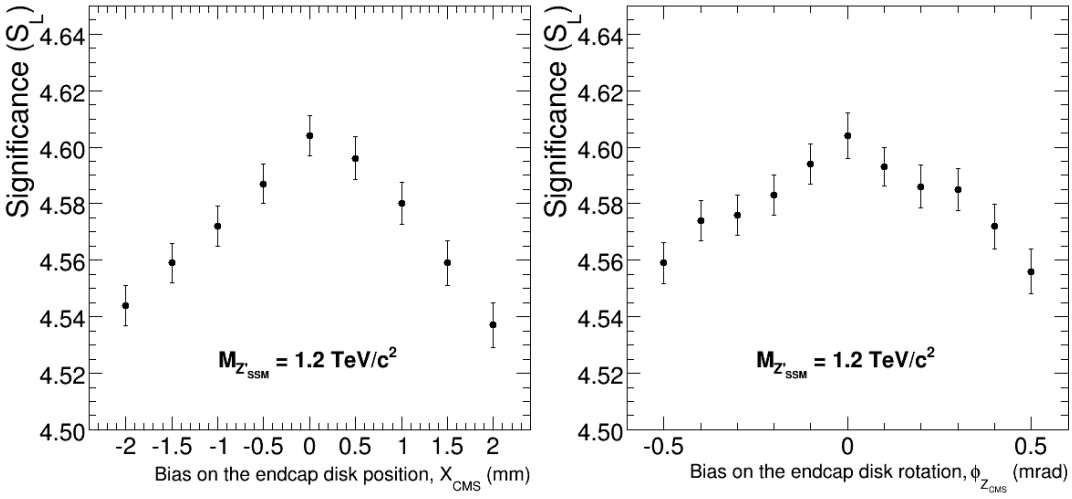

Figure 4.17: Average Z'_{SSM} signal significance as a function of the bias on the x_{CMS} position (left) and rotation around the beam line (right) of the muon endcap disks for $M_{Z'_{SSM}} = 1.2$ TeV/c^2 using ideal alignment.

4.7 Summary

Monte Carlo signal samples for $Z'_{SSM} \rightarrow \mu^+\mu^-$ in pp collisions at 7 TeV center-of-mass energy are generated and reconstructed for different Z' masses (1 TeV/c^2, 1.2 TeV/c^2, 1.3 TeV/c^2, and 2 TeV/c^2) with three different alignment scenarios. Two Monte Carlo samples for the dominant and irreducible Drell-Yan background are also generated for $M_{\mu^+\mu^-} > 200$ GeV/c^2 and $M_{\mu^+\mu^-} > 500$ GeV/c^2. The $50\,pb^{-1}$ alignment scenario is validated with this study. The muon transverse momentum and the dimuon mass resolutions are calculated with three muon reconstructions for the combinations of alignment scenarios, center-of-mass energies for different Z' masses. We find the global muon momentum resolution in the endcap 14.4% (4.8%) with the startup (ideal) alignment using the 1.2 TeV/c^2 Z'_{SSM} sample. The dimuon mass resolution is found to be 10.3% (3.2%) for the startup (ideal) alignment using the 1.2 TeV/c^2 Z'_{SSM} sample. An alignment systematics study is accomplished by varying the position or orientation of endcap stations with respect to ideal or startup alignment scenarios. We find a symmetrical effect on resolution with positive bias or negative bias and similar results for biases in x_{CMS} or y_{CMS}, when using the ideal alignment scenario, but not with the startup alignment scenario, which produces asymmetrical results. With the bias in z_{CMS} applied to all stations together, the resolution stays the same as without bias. With a misalignment of 2 mm

in x_{CMS} or y_{CMS} position on ideal alignment scenario of all stations, the p_T resolution in the endcap worsens by about 2%.

We evaluate the discovery potential for $Z' \rightarrow \mu^+\mu^-$ in pp collisions at 7 TeV center-of-mass energy for different muon misalignments. We calculate the Z'_{SSM} signal significance as a function of integrated luminosity and estimate the required data for 5σ for two signal mass points. About 80 pb^{-1} of data and at least 250 pb^{-1} data with an aligned detector are required to discover a Z'_{SSM} with mass M = 1 TeV/c^2 and 1.2 TeV/c^2, respectively. Finally, we study the effect of muon endcap only misalignments on the Z' search and find a very small effect on the Z'_{SSM} signal significance.

Chapter 5

CMS Collision Data Analysis

5.1 CMS Collision Data

In the first three and half months of LHC [8] operation at $\sqrt{s} = 7$ TeV, the LHC has delivered 346 nb^{-1} of proton-proton collision data and CMS has recorded 303 nb^{-1} of the data [59] as shown in Figure 5.1 (from Ref. [59]). I have analyzed the collision data, mostly the dimuon data recorded from March 30, 2010 to July 19, 2010.

5.2 Dimuon Data Analysis

The CMS dimuon data are analyzed using "Zprime2Muanalysis" code [43]. Data selections, event selections, and results are presented in the following sections:

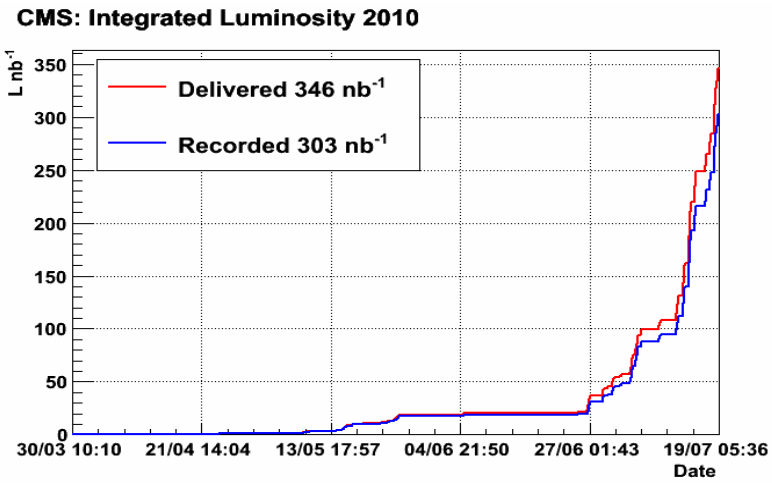

Figure 5.1: Integrated luminosities delivered by LHC during the first three and half months of data taking at $\sqrt{s} = 7$ TeV and recorded by CMS up to the Run 139121 are shown in red and blue, respectively.

5.2.1 Data Selections

The following CMS datasets are used for the analysis:

1. /MinimumBias/Commissioning10-CS_Onia-Jun14thSkim_v1/RAW-RECO

   135,740 Events; Runs 131511-135802 (Dates: March 30 - April 15, 2010)

2. /Mu/Run2010A-CS_Onia-Jun14thSkim_v1/RAW-RECO

   79,833 Events; Runs 135821-137436 (Dates: April 15 - June 10, 2010)

3. /Mu/Run2010A-PromptReco-v4/RECO

   99,979,833 Events; Runs 137437-140399 (Dates: June 10 - July 19, 2010)

These datasets have not yet passed the data certification mechanism in this analysis chain. The analysis chain starts basically with an input dataset, analysis codes, and a user-defined configuration file to create jobs in order to analyze data at various grid sites where the datasets are available. These jobs are created, submitted, and finally retrieved by using the CMS Remote Analysis Builder (CRAB). While analyzing the datasets using the CRAB, data collected during good runs which are listed in a file, called as JavaScript Object Notation (JSON) file, are processed. The official JSON file [60] provides a list of good runs. Good runs indicate the CMS sub-detectors were running properly and the data collected during these runs are actually the collision events. So, the procedure reduces heavily the data to analyze and confirms that the various CMS sub-detectors were running properly during the range of runs. Specifically, I have used the following JSON file available for CMS users in the official location [60]: StreamExpressCert_132440-140399_7TeV_StreamExpress_Collisions10_JSON.txt.

For these skimmed datasets and good runs/events, the integrated luminosities of processed data are 4.71 nb^{-1}, 5.42 nb^{-1}, and 122.96 nb^{-1}, respectively, for the three datasets mentioned above in Section 5.2.1.

5.2.2 Event Selections

The event selection is slightly modified from that described in 4.3 in order to accommodate actual collision data and low p_T muons for early data. For selecting events in real data, it is required that

- The transverse momentum p_{T} of each muon track in a pair of oppositely-charged muons be larger than 1 GeV/c;
- Both muons be isolated in the tracker in such a way that the sum of the p_{T} of all tracks around each muon in a cone of $\Delta R < 0.3$ is required to be less than 10 GeV/c;
- There be a good primary vertex; i.e a primary vertex (not fake) with at least four tracks and with the z-coordinate of the point of closest approach of the tracks to the z-axis i.e. $|z| \leq 15$ cm and radius $|\rho| \leq 2$ cm. The code can be found in [61].
- The fraction of high purity tracks with more than 10 tracks in the event be at least 0.25. The code can be found in [61].

5.2.3 Results

Dimuon Mass Spectra

The reconstructed invariant mass spectrum for dimuons satisfying the selection criteria is shown in Figure 5.2. The known low mass resonaces are shown. In Figure 5.3, these low mass resonances are shown separately in detail: (a) J/ψ, (b) Υ, and (c) Z are observed at about 3.1 GeV/c^2, 9.5 GeV/c^2, and 91 GeV/c^2, respectively. Bin sizes and ranges are varied to visualize peaks distinctly.

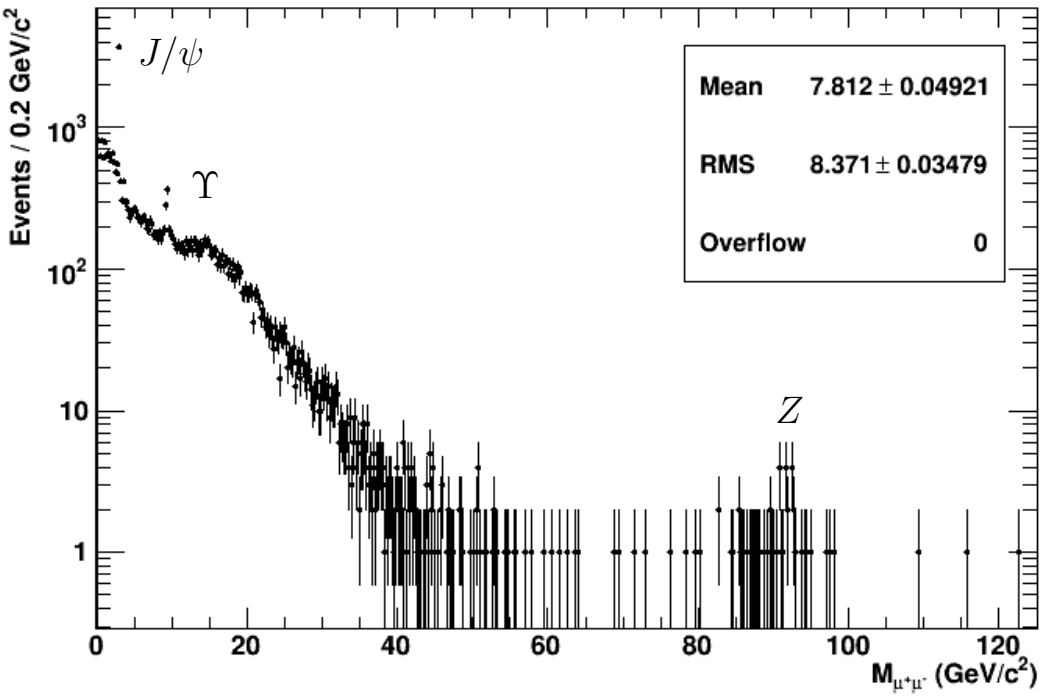

Figure 5.2: Dimuon mass spectrum of the CMS collision data collected during March 30 - July 19, 2010 at $\sqrt{s} = 7$ TeV.

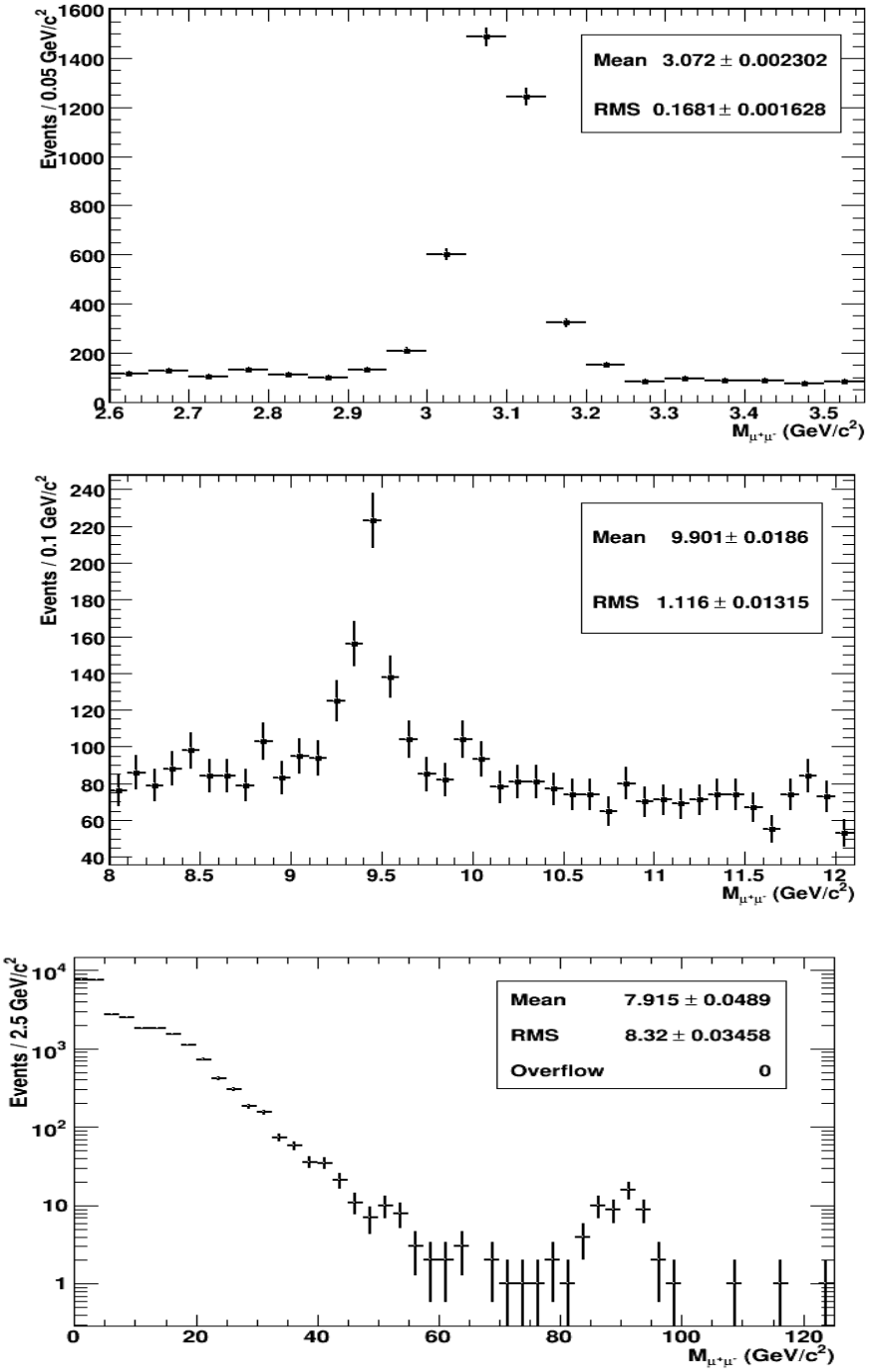

Figure 5.3: Distributions of the dimuon mass showing low mass resonance peaks: J/ψ (top), Υ (center), and Z (bottom).

Comparison with MC

The distribution of mass for reconstructed dimuons from the collision data at $\sqrt{s} = 7$ TeV are compared with the corresponding variable from the simulated events for $Z \rightarrow \mu^+\mu^-$ normalized with the number of events from data in Figure 5.4. Data from the very early collision data in the Z range agree well within statistics with MC expectations. The highest dimuon mass observed so far is 123 GeV/c^2 shown in Figure 5.3(bottom).

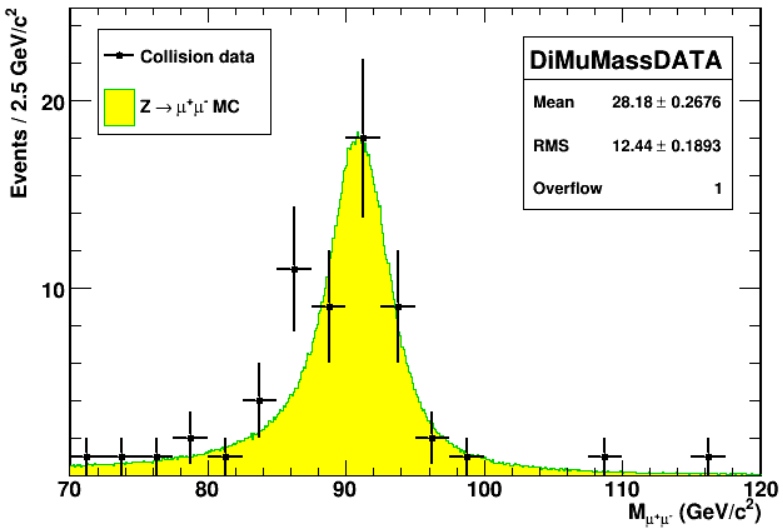

Figure 5.4: Comparison of the dimuon mass from the collision data at $\sqrt{s} = 7$ TeV with simulated MC events for $Z \rightarrow \mu^+\mu^-$.

5.3 Summary

About 300 nb^{-1} of proton-proton collision data taken through July 19, 2010 at $\sqrt{s} = 7$ TeV with the CMS experiment are analyzed. For the first time, the performance of the CMS dimuon reconstruction for collision data has been analyzed using "Zprime2Muanalysis" code. In the dimuon mass spectrum, low mass resonance peaks J/ψ, Υ, and Z appear as expected. The dimuon mass spectrum around Z is compared with simulated events for $Z \rightarrow \mu^+\mu^-$. In general the agreement between data and predictions from the simulation is reasonably good over the Z region for these early data. However, the experiment is still in the commissioning phase of the search for high-mass resonances and higher confidence results can soon be expected.

Chapter 6

Conclusions and Outlook

Conclusions

The muon endcap alignment system worked reasonably well in the early commissioning phase. As a result, a partially-aligned muon endcap geometry at B = 3.8 T has been delivered to CMS. The precisions obtained so far for the ME2, ME3, and ME4 chambers (about 300 μm in z_{CMS} and 200 μrad in $\phi_{x_{\mathrm{local}}}$) are close to those required by CMS. The present work establishes a major milestone towards obtaining a fully aligned detector geometry.

The alignment systematics study is a unique contribution to the Z' analysis. Using the MC samples, the muon transverse momentum and the dimuon mass resolutions for various misalignment scenarios are quantified systematically. The 50 pb^{-1} alignment scenario is validated by this study. My results show the

small effect of muon endcap misalignments on the resolutions and on the Z' signal significance. The study describes various muon endcap misalignment scenarios and their impact on p_T resolution in the endcap and on the Z'_{SSM} signal significance.

This evaluation of the discovery potential for $Z' \rightarrow \mu^+\mu^-$ in pp collisions at 7 TeV center-of-mass energy for different muon misalignments estimates the required data for a 5σ discovery for the signal mass points just above the current lower mass limit, i.e. 1030 GeV/c^2. This study also estimates how the Z' signal peak gets widened with various muon misalignments and the possible impact on the statistical significance. A 1050 GeV/c^2 Z'_{SSM} signal could be detected when $\sim 100\, pb^{-1}$ data are collected and analyzed, using a CMS detector geometry aligned with at least 50 pb^{-1} data. The negligible effect of muon endcap systematic misalignments up to 2 mm or 0.5 mrad on the Z' signal significance builds confidence that the Z' signal would not disappear in the dimuon spectrum because of misalignment of muon endcaps.

The analysis results of very early CMS collision data of about 300 nb^{-1} are promising. The results show the established low mass peaks of J/ψ, Υ, and Z in the dimuon channel with the CMS experiment. The search for high-mass resonances is in progress.

Possible Future Work

The detector must be re-aligned if there is any opening and re-closing of the yoke disks. Experience from the currently ongoing work shows that such interventions are happening regularly. Consequently, the alignment has to be redone many times, but simply running the codes developed by the author with slight modifications of input data produces acceptable results. The detector alignment in z_{CMS} and $\phi_{x_{\mathrm{local}}}$ has already been done with data recorded in 2009 and 2010. In fact, the alignment of the CSC chambers for the remaining degrees of freedom, in particular for x_{CMS} and y_{CMS}, which are crucial for momentum reconstruction, is already in final shape as an extension of the present work. In the end, CMS needs the aligned geometry of the detector in all degrees of freedom.

CMS will certainly offer good chances to explore the mass region above 1 TeV/c^2 for the Z' search. Data will show if nature has decided to create it. Once a Z' boson is discovered, its observables can be used in the attempt to identify the theoretical model to which it belongs. The measurement of the forward-backward asymmetries of leptonic decay products, both at the resonance peak and off the peak, will be a powerful tool to identify the correct model [51]. If no Z' signal is found, the current 95 % C. L. lower mass limit for Z' could be improved with data collected in the first year of running.

Bibliography

[1] D. Griffiths, "Introduction to Elementary Particles," *John Wiley Sons* (1987).

[2] F. Halzen and A. Martin, "Quarks and Leptons," *John Wiley Sons* (1984).

[3] LEP Experiments, http://greybook.cern.ch/.

[4] **CDF** Collaboration, T. Aaltonen et al., "Search for High-Mass Resonances Decaying to Dimuons at CDF," *Phys. Rev. Lett.* **102** (2009) 091805, arXiv:arXiv:0811.0053v2.

[5] P. Langacker, "The Physics of Heavy Z' Gauge Bosons," *Rev. Mod. Phys.* **81** (2008) 1199–1228, arXiv:0801.1345.

[6] P. Langacker, "Z' Physics at the LHC," arXiv:0911.4294.

[7] CMS Collaboration, "The CMS experiment at the CERN LHC," *J. Inst* **0803** (2008) S08004. doi:10.1088/1748-0221/3/08/S08004.

[8] L. Evans, (ed.) and P. Bryant, (ed.), "LHC Machine," *J. Inst* **3 (S08001)** (2008). doi:10.1088/1748-0221/3/08/S08001.

[9] CMS Collaboration, "The Muon Project Technical Design Report," *CERN Report CERN/LHCC* **97-32** (1997).

[10] **CMS** Collaboration, "CMS Technical Design Report, Vol. II: Physics Performance," *J. Phys.* **G 34** (2007) 995.

[11] **D0** Collaboration, V. M. Abazov et al., "Search for a heavy neutral gauge boson in the dielectron channel with 5.4 fb^{-1} of $\mathbf{p\bar{p}}$ collisions at $\sqrt{\mathbf{s}} = \mathbf{1.96}$ TeV," arXiv:1008.2023.

[12] **LHC** Collaboration, "LHC Design Report," *CERN/LHCC* **03** (2004).

[13] **CMS** Collaboration, "The muon project technical design report," *CERN/LHCC* **97-032** (1997).

[14] Large Hadron Collider, http://en.wikipedia.org/wiki/Large_Hadron_Collider.

[15] The LHC Experiments, CERN, http://public.web.cern.ch/public/en/LHC/LHCExperiments-en.html.

[16] **CMS** Collaboration, "Physics Technical Design Report, Vol. 1: Detector Performance and Software," *CERN/LHCC* **2006-001** (2006).

[17] **CMS** Collaboration, "The CMS experiment at the CERN LHC, Journal of Instrumentation," *Journal of Instrumentation* **3** (2008).

[18] ATLAS Collaboration, http://atlas.web.cern.ch/Atlas/index.html.

[19] LHCb Collaboration, http://lhcb.web.cern.ch/lhcb/.

[20] ALICE Collaboration, http://aliceinfo.cern.ch/.

[21] Compact Muon Solenoid Experiment, http://cmsinfo.cern.ch/.

[22] CMS detector overview, http://cms.web.cern.ch/cms/Detector/FullDetector/index.html.

[23] **CMS** Collaboration, "CMS Tracker Project, Technical Design Report," *CERN/LHCC* **98-6** (1998).

[24] **CMS** Collaboration, "The Magnet Project Technical Design Report," *CERN/LHCC* **97-010** (1997).

[25] M. Hohlmann et al., "Aligning the CMS Muon Endcap Detector with a System of Optical Sensors," *Proc. IEEE Nucl. Sci. Symp. 2007, Honolulu, USA; CMS Conference Report* **CR-2008-015** (2008).

[26] CMS Collaboration, "Commissioning of the CMS Experiment and the Cosmic Run at Four Tesla," *J. Inst.* **5** (Nov, 2009) T03001. doi:10.1088/1748-0221/5/03/T03001.

[27] CMS Collaboration, "Alignment of the CMS muon system with cosmic-ray and beam-halo muons," *J. Instrum.* **5** (Nov, 2009) T03020. doi:10.1088/1748-0221/5/03/T03020.

[28] CMS Collaboration, "Aligning the CMS Muon Chambers with the Muon Alignment System during an Extended Cosmic Ray Run," *J. Instrum.* **5** (Nov, 2009) T03019. 35 p. doi:10.1088/1748-0221/5/03/T03019.

[29] P. Arce and A. López-Virto, "CMS Object Oriented Code for Optical Alignment (COCOA)," *CMS Note* **2002/060** (2002).

[30] P. Arce, "Object Oriented Software for Simulation and Reconstruction of Big Alignment Systems," *Proc. of 7th International Workshop on Accelerator Alignment (IWAA), Spring-8, Japan* (2002).

[31] P. Arce, "Object Oriented Software for Simulation and Reconstruction of Big Alignment Systems," *Proc. of 6th International Workshop on Accelerator Alignment (IWAA), Grenoble, France* (1999).

[32] M. Hohlmann et al., "Design and Performance of the Alignment System for the CMS Muon Endcaps," *Proc. IEEE Nucl. Sci. Symp. 2006, San Diego, USA; CMS Conference Report* **CR-2008-016** (2008).

[33] CMS Collaboration, "Performance of the CMS Cathode Strip Chambers with Cosmic Rays," *J. Instrum.* **5** (Nov, 2009) T03018. doi:10.1088/1748-0221/5/03/T03018.

[34] R. H. Lee, "SIMULATION AND STUDY OF THE CMS ENDCAP MUON ALIGNMENT SCHEME," *A Ph.D. thesis submitted to Purdue University* (May, 2002).

[35] R. Goudard, J.D. Maillefaud, and A. Maurisset, "CMS-Yoke Endcaps Opening of all the Endcaps position check after CRAFT," *Survey Report, EDMS 982666* **CMS-SG-UR-0124** (2009).

[36] L.A. Garcia-Moral et al., "Motions of CMS Detector structures due to the magnetic field forces as observed by the Link Alignment System during the test of the 4 Tesla magnet solenoid," *Nucl. Inst. Meth.* **A606** (2009) 3. doi:10.1016/j.nima.2009.03.252.

[37] CMS Collaboration, "Performance of CMS Muon Reconstruction in Cosmic-Ray Events," *J. Instrum.* **5** (Nov, 2009) T03022. doi:10.1088/1748-0221/5/03/T03022.

[38] Global Tags for Conditions Data, https://twiki.cern.ch/twiki/bin/viewauth/CMS/SWGuideFrontierConditions.

[39] Available Alignment Constants,
https://twiki.cern.ch/twiki/bin/view/CMS/SWGuideAlignmentConstants.

[40] Scenarios for Mis-Alignment and Mis-Calibration for Monte Carlo Production, https://twiki.cern.ch/twiki/bin/view/CMS/AlCaScenarios.

[41] 50 pb^{-1} muon misalignment scenario (MC),
https://hypernews.cern.ch/HyperNews/CMS/get/muon-alignment/342.html.

[42] Tracker Misalignment Scenarios,
https://twiki.cern.ch/twiki/bin/view/CMS/TkMisalignmentScenariosCSA07.

[43] Zprime2muAnalysis package,
http://cmssw.cvs.cern.ch/cgi-bin/cmssw.cgi/CMSSW/SUSYBSMAnalysis/Zprime2muAnalysis/.

[44] CMS Collaboration, "CMS Technical Design Report, Volume II: Physics Performance," *J. Phys.* **G34** (2007) 995–1579.

[45] R. Cousins, J. Mumford, and V. Valuev, "Detection of Z' Gauge Bosons in the Dimuon Decay Mode in CMS," *CMS Note* **2006/062** (2006).

[46] I. Belotelov et al., "Search for Randall-Sandrum Graviton Decay into Muon Pairs," *CMS Note* **2006/104** (2006).

[47] V. Valuev, "Evaluation of CMS Discovery Potential in the $Z' \to \mu^+\mu^-$ Channel at $\sqrt{s} = 6$ and 10 TeV," *CMS AN Note* **2009/017** (2009).

[48] T. Sjostrand, S. Mrenna, and P. Skands, "PYTHIA 6.4 physics and manual," *JHEP* **05** (2006) 026, arXiv:hep-ph/0603175v2.

[49] J. Pumplin et al., "New generation of parton distributions with uncertainties from global QCD analysis," *JHEP* **07** (2002) 012, arXiv:hep-ph/0201195.

[50] M. R. Whalley, D. Bourilkov, and R. C. Group, "The Les Houches Accord PDFs (LHAPDF) and Lhaglue," arXiv:hep-ph/0508110.

[51] P. Langacker, R. W. Robinett, and J. L. Rosner, "New heavy gauge bosons in pp and $p\bar{p}$ collisions," *Phys. Rev. D* **30** (Oct, 1984) 1470–1487. doi:10.1103/PhysRevD.30.1470.

[52] CMSSW Reference Manual, https://cms-cpt-software.web.cern.ch/cms-cpt-software/General/gendoxy-doc.php.

[53] MC Samples at Florida Tech, https://cmsweb.cern.ch/dbs_discovery/aSearch?caseSensitive=onuserMode=user&sortOrder=descsortName=&grid=0method=dbsapidbsInst=cms_dbs_ph_analysis_02&userInput=find+dataset+where+site+like+*FLTECH*.

[54] CMS Collaboration, "The CMS Physics Technical Design Report, Volume I," *CERN/LHCC* **2006-001** (2006).

[55] M. Chen et al., "Search for New High-Mass Resonances Decaying to Muon Pairs in the CMS Experiment," *CMS AN* **2007/038** (2007).

[56] J. Pivarski et al., "Confirmation of the Effect of RPC Hits and Updated Alignment without RPC Bias," *CMS Muon Alignment Meeting* (2010). (28 May, 2010).

[57] Software Guide for Muon Geometry Conversion, https://twiki.cern.ch/twiki/bin/viewauth/CMS/SWGuideMuonGeometryConversion.

[58] R. Cousins, J. Mumford, and V. Valuev, "Detection of Z' Gauge Bosons in the Dimuon Decay Mode in CMS," *CMS Note* **2005/002** (2005).

[59] Approved 2010 CMS Lumi plots, https://twiki.cern.ch/twiki/bin/view/CMS/LumiWiki2010Approveddata.

[60] Data Certification Schedule towards ICHEP, https://twiki.cern.ch/twiki/bin/viewauth/CMS/ICHEPDataCertSchedule.

[61] Recipes for the analysis of the data from 7TeV collision of 2010, https://twiki.cern.ch/twiki/bin/viewauth/CMS/Collisions2010Recipes.